

# High-Throughput Condensed-Phase Hybrid Density Functional Theory for Large-Scale Finite-Gap Systems: The **SeA** Approach

Hsin-Yu Ko,<sup>1</sup> Marcos F. Calegari Andrade,<sup>2</sup> Zachary M. Sparrow,<sup>1</sup> and Robert A. DiStasio Jr.<sup>1,\*</sup>

<sup>1</sup>*Department of Chemistry and Chemical Biology, Cornell University, Ithaca, NY 14853, USA*

<sup>2</sup>*Department of Chemistry, Princeton University, Princeton, NJ 08544, USA*

(Dated: August 15, 2022)

High-throughput electronic structure calculations (often performed using density functional theory (DFT)) play a central role in screening existing and novel materials, sampling large swaths of potential energy surfaces, and generating quantum mechanical data for machine learning applications. By including a fraction of exact exchange (EXX), hybrid functionals reduce the self-interaction error in semi-local DFT and furnish a more accurate description of the underlying electronic structure, albeit at a high computational cost that often prohibits such high-throughput applications. To address this challenge, we have constructed a robust, accurate, and computationally efficient framework for high-throughput condensed-phase hybrid DFT based on `exx`—a linear-scaling EXX algorithm that exploits the sparsity between localized orbitals in real space to enable hybrid DFT calculations on large-scale finite-gap systems. The resulting **SeA** approach ( $\text{SeA} = \text{SCDM} + \text{exx} + \text{ACE}$ ) combines and seamlessly integrates: (i) the selected columns of the density matrix (SCDM) method (a robust and non-iterative orbital localization scheme that sidesteps the need for system-dependent optimization protocols), (ii) a recently extended version of `exx` (a black-box algorithm for accurately and efficiently evaluating the action of the standard/full-rank EXX operator ( $\hat{V}_{\text{xx}}$ ) based on a single system-independent orbital coverage threshold), and (iii) adaptively compressed exchange (ACE) (an efficient low-rank  $\hat{V}_{\text{xx}}$  approximation that eliminates unnecessary full-rank evaluations of the action during the iterative self-consistent field (SCF) procedure). In doing so, **SeA** is able to harness three levels of computational savings during hybrid DFT calculations: two from  $\text{SCDM} + \text{exx}$  (*pair selection* and *domain truncation*: by only considering spatially overlapping orbital pairs and evaluating their corresponding EXX interaction on orbital-pair-specific/system-size-independent real-space domains) and one from ACE (*low-rank  $\hat{V}_{\text{xx}}$  approximation*: by reducing the number of full-rank evaluations of the action (via calls to  $\text{SCDM} + \text{exx}$ ) during the SCF procedure). By considering a diverse set of 200 non-equilibrium  $(\text{H}_2\text{O})_{64}$  configurations (including intact and auto-ionized water molecules, with densities spanning  $0.5 \text{ g/cm}^3$ – $1.5 \text{ g/cm}^3$ ), **SeA** yields an order-of-magnitude ( $\approx 20\times$ ) speedup in the rate-determining step in the convolution-based ACE implementation in Quantum ESPRESSO while reproducing the EXX energy and ionic forces with high fidelity (i.e., median energy errors of  $\approx 10^{-3}\%$  and ionic force errors that are lower than typical structural relaxation thresholds). In doing so, **SeA** effectively removes the computational bottleneck that prohibits the routine use of hybrid DFT in high-throughput applications, providing an  $\approx 6\times$  speedup in the overall cost of the ACE algorithm (and  $\gtrsim 100\times$  overall speedup when compared to the conventional EXX implementation) for systems similar in size to  $(\text{H}_2\text{O})_{64}$ . As a proof-of-principle high-throughput application, we used **SeA** to train a deep neural network (DNN) potential for ambient ( $T = 300 \text{ K}$ ,  $p = 1 \text{ Bar}$ ) liquid water at the hybrid (PBE0) DFT level, leading to a final actively learned data set containing  $\approx 8,000$   $(\text{H}_2\text{O})_{64}$  configurations. Using an out-of-sample test set ( $(\text{H}_2\text{O})_{512}$  at  $T = 330 \text{ K}$ ,  $p = 1 \text{ Bar}$ ), we confirmed the accuracy of the **SeA**-trained DNN potential and showcased the capability of **SeA** by directly computing the ground-truth ionic forces in this challenging system containing  $> 1,500$  atoms.

## I. INTRODUCTION

High-throughput *ab initio* electronic structure calculations play a key role in the computational screening and design of novel materials,<sup>1,2</sup> exploring and sampling potential energy surfaces (PES), as well as generating quantum mechanical data needed for machine learning (ML) applications.<sup>3–5</sup> Since the accuracy of such high-throughput calculations is largely governed by the underlying electronic structure method, it is crucial to perform these calculations at an appropriate level of theory. Among the available *ab initio* electronic structure methods, Kohn-Sham (KS) density functional theory (DFT)<sup>6,7</sup> has emerged as the computational workhorse

for simulating large molecules and complex condensed-phase systems. Despite being exact in theory, the exchange-correlation (xc) functional encoding the non-trivial many-body interactions between electrons remains unknown to date; hence, the accuracy of DFT calculations in practice largely relies on functional approximations.<sup>8–16</sup> For condensed-phase systems, the xc functional is predominantly computed within the (semi-local) generalized gradient approximation (GGA), which includes a local dependence on the electron density,  $\rho(\mathbf{r})$ , and its gradient,  $\nabla\rho(\mathbf{r})$ . To reduce the deleterious self-interaction error (SIE)<sup>17,18</sup> at the GGA level (in which each electron spuriously interacts with itself), hybrid functionals<sup>19</sup> include a fraction of exact exchange (EXX) in the xc contribution to the DFT energy. In doing so,

hybrid functionals tend to furnish a more accurate description of the underlying electronic structure, albeit at a high computational cost that often limits their use in high-throughput applications (particularly for large-scale condensed-phase systems).

Since the cost of performing condensed-phase hybrid DFT calculations using the conventional convolution-based EXX algorithm<sup>20</sup> often significantly exceeds that of GGA-based KS-DFT, methods for efficiently performing such challenging calculations are key to the routine use of hybrid functionals in high-throughput applications and have received considerable attention from the community.<sup>21–49</sup> For large-scale condensed-phase systems with finite gaps, a numerically accurate evaluation of the EXX energy ( $E_{\text{xx}}$ ) can be accomplished with linear-scaling cost using `exx`,<sup>47,49</sup> a real-space algorithm that exploits the sparsity in the exchange interaction provided by a localized representation of the occupied orbitals (e.g., maximally localized Wannier functions, MLWFs).<sup>50,51</sup> To facilitate a linear-scaling (or order- $N$ ) evaluation of  $E_{\text{xx}}$  (as well as other important EXX-related quantities, *vide infra*), the `exx` algorithm exploits the following two levels of sparsity (for more details, see Sec. II B and Refs. 47 and 49): (i) pair selection—`exx` only considers spatially overlapping orbital pairs that will have a non-vanishing EXX interaction and (ii) domain truncation—`exx` only evaluates the corresponding EXX interaction on an orbital-pair-specific/system-size-independent spatial domain (instead of the entire real-space mesh). With a massively parallel hybrid MPI/OpenMP implementation in the CP module of the open-source Quantum ESPRESSO (QE) package<sup>52</sup> in conjunction with on-the-fly MLWF localization,<sup>53</sup> `exx` has enabled hybrid DFT based *ab initio* molecular dynamics (AIMD) of large-scale condensed-phase systems containing 500–1000 atoms in the microcanonical/canonical ( $NVE/NVT$ ) and isobaric-isenthalpic/isobaric-isothermal ( $NpH/NpT$ ) ensembles with a wall time cost that is comparable to GGA-based KS-DFT.<sup>47,49</sup> In doing so, current (and pilot) implementations of `exx` have been used to conduct several challenging theoretical investigations at the hybrid DFT level regarding the electronic structure of semi-conducting solids,<sup>54,55</sup> the structure and local order of ambient liquid water,<sup>33,56</sup> the structural and dynamical properties of aqueous ionic solutions,<sup>57,58</sup> the thermal properties of the pyridine-I molecular crystal,<sup>59</sup> as well as isotope effects on the structure of liquid water.<sup>60</sup>

While the current implementation of `exx`<sup>47,49</sup> was designed for large-scale AIMD simulations (particularly the Car–Parrinello<sup>61</sup> or CPMD variant), the computational efficiency of the core `exx` algorithm also makes it well-suited for rapidly evaluating the action of the EXX operator ( $\hat{V}_{\text{xx}}$ ) on the (proto-)KS orbitals ( $\{\phi_i\}$ ) during high-throughput self-consistent field (SCF) calculations at the hybrid DFT level (i.e.,  $\hat{V}_{\text{xx}}\phi_i$ , which is equivalent (to within a sign) to the EXX contribution to the wavefunction forces needed to propagate the CPMD equations of motion, see Sec. II B). However, direct use of

this version of `exx` would not meet the *implicit* robustness requirements of a high-throughput framework (i.e., black-box and automatable algorithms), since this implementation contains system-dependent parameters in: (i) the optimization protocol used to iteratively obtain the MLWFs needed by `exx` (e.g., initial guesses, convergence criteria, choice of optimization algorithm), and (ii) the pair-selection and domain-truncation protocols used inside `exx`<sup>47,49</sup> to harness the aforementioned two levels of computational savings (i.e., the pair distance cutoff, Poisson equation radii, and multipole expansion radii). In addition to these robustness requirements, there is potentially a third level of computational savings that could be harnessed to increase the efficiency of high-throughput SCF calculations at the hybrid DFT level. As pointed out by Lin,<sup>36</sup> these savings result from replacing unnecessary evaluations of  $\hat{V}_{\text{xx}}\phi_i$  using the standard/full-rank EXX operator—the typical bottleneck during SCF calculations at the hybrid DFT level—with computationally more efficient evaluations of the action using a low-rank approximation for  $\hat{V}_{\text{xx}}$  (i.e., the adaptively compressed exchange (ACE) operator).

In this work, we directly address these issues by combining and seamlessly integrating three theoretical and algorithmic advances into a robust, accurate, and computationally efficient framework for performing high-throughput condensed-phase hybrid DFT calculations on large-scale finite-gap systems. As depicted in Fig. 1, the resulting SeA framework (SeA = SCDM+`exx`+ACE) includes the selected columns of the density matrix (SCDM) orbital localization scheme of Damle, Lin, and Ying,<sup>35</sup> a recent black-box extension<sup>62</sup> to our linear-scaling `exx` algorithm,<sup>47,49</sup> and the ACE formalism of Lin.<sup>36</sup> For an accurate and efficient evaluation of the action using the standard/full-rank EXX operator—the typical bottleneck during SCF calculations at the hybrid DFT level—SeA employs the non-iterative SCDM procedure for localized orbital generation (thereby eliminating the need for system-dependent optimization protocols) in conjunction with a recently extended black-box version<sup>62</sup> of `exx` that replaces all system-dependent parameters with a single system-*independent* orbital coverage threshold. As described in Ref. 62, this version of `exx` is quite robust and able to treat both homogeneous and heterogeneous (i.e., multi-phase and/or multi-component) systems with controllable accuracy (i.e., with a finite and *a priori* determined error) and markedly improved computational efficiency. Hence, the combined use of SCDM with this version of `exx` (SCDM+`exx`) forms an effectively black-box EXX engine that harnesses two levels of computational savings (i.e., pair selection and domain truncation) when evaluating the most computationally demanding step in hybrid DFT (i.e.,  $\hat{V}_{\text{xx}}\phi_i$ ). To further improve the overall efficiency, SeA employs the ACE formalism to reduce the number of times that  $\hat{V}_{\text{xx}}\phi_i$  needs to be evaluated during the iterative SCF procedure, thereby harnessing a third level of computational savings. In doing so, SeA not only reduces the num-

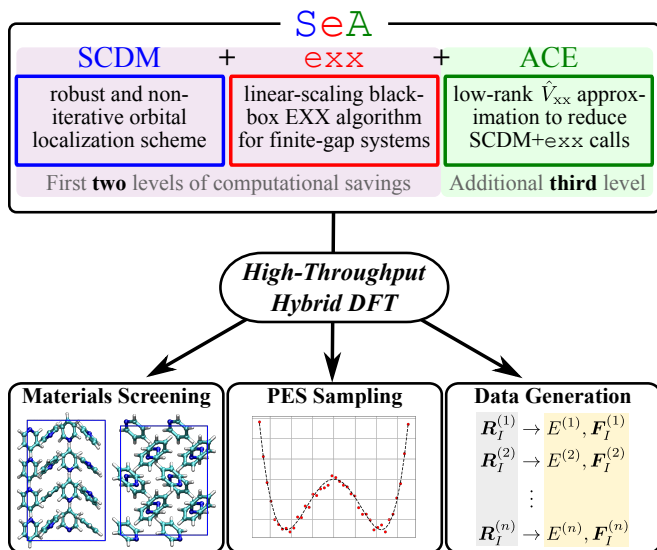


FIG. 1. Schematic illustration of the SeA approach, which seamlessly integrates three theoretical and algorithmic advances (the non-iterative selected columns of the density matrix (SCDM) orbital localization scheme,<sup>35</sup> the linear-scaling exx algorithm,<sup>47,49,62</sup> and the adaptively compressed exchange (ACE) formalism<sup>36</sup>) into a robust, accurate, and computationally efficient framework for performing high-throughput condensed-phase hybrid DFT calculations on large-scale finite-gap systems. By harnessing three levels of computational savings, SeA paves the way towards the routine use of hybrid DFT in high-throughput applications such as materials screening and discovery, potential energy surface (PES) sampling, and data generation for machine learning (ML).

ber of calls to the most computational demanding step in hybrid DFT calculations (via ACE), but also drastically reduces the cost of evaluating each of the remaining calls (via SCDM+exx). Inspired by the pioneering work of Dawson and Gygi,<sup>34</sup> Giannozzi and coworkers,<sup>43</sup> and Nair and coworkers,<sup>44,45</sup> SeA differs from this previous work (which improved the efficiency of hybrid DFT by harnessing one or two levels of computational savings via pair selection and ACE) by providing a single framework that harnesses three levels of savings (pair selection, domain truncation, and ACE) to further enable the routine use of hybrid DFT in high-throughput applications involving large-scale condensed-phase systems.

The remainder of this manuscript is organized as follows. In Sec. II, we provide a brief review of the SCDM, exx, and ACE approaches as well as their seamless integration into the SeA framework. In Sec. III, we assess the accuracy and performance of SeA on a diverse set of 200 non-equilibrium  $(\text{H}_2\text{O})_{64}$  configurations (including intact and auto-ionized water molecules, with densities spanning 0.5 g/cm<sup>3</sup>–1.5 g/cm<sup>3</sup>), and demonstrate that SeA yields an order-of-magnitude ( $\approx 20\times$ ) speedup in the rate-determining step in the convolution-based ACE implementation in PWSCF while reproduc-

ing the EXX energy and ionic forces with high fidelity. In doing so, SeA effectively removes the computational bottleneck that prohibits the routine use of hybrid DFT in high-throughput applications for systems with sizes similar to (and beyond)  $(\text{H}_2\text{O})_{64}$ , and enables single-point energy and ionic force evaluations for such systems with an  $\approx 6\times$  overall speedup compared to the ACE algorithm (and  $\gtrsim 100\times$  compared to the conventional convolution-based EXX implementation). As a proof-of-principle high-throughput application, we used SeA in Sec. IV to train a deep neural network (DNN) potential for ambient ( $T = 300$  K,  $p = 1$  Bar) liquid water at the PBE0<sup>63,64</sup> level based on an actively learned data set containing  $\approx 8,000$   $(\text{H}_2\text{O})_{64}$  configurations. We then assessed the accuracy of this DNN potential on an out-of-sample test set ( $(\text{H}_2\text{O})_{512}$  at  $T = 330$  K and  $p = 1$  Bar), and showcased the capabilities of SeA by directly computing the (ground truth) ionic forces in these challenging condensed-phase systems containing  $> 1,500$  atoms. This manuscript is ended with a brief summary of our findings and some potential future research directions in Sec. V.

## II. THEORY

In this section, we begin with a brief review of the non-iterative SCDM orbital localization scheme,<sup>35</sup> which will be used to generate localized occupied orbitals without the need for system-dependent optimization protocols (Sec. II A). With localized orbitals in hand, we then describe a recent extension<sup>62</sup> to the linear-scaling exx algorithm<sup>47,49</sup> which replaces all system-dependent parameters with a single system-independent orbital coverage threshold (Sec. II B); this algorithm harnesses two levels of computational savings (i.e., pair selection and domain truncation) and will be used to provide an accurate and efficient black-box evaluation of the action using the standard/full-rank EXX operator ( $\hat{V}_{xx}$ ). We then briefly summarize the ACE method, which harnesses a third level of computational savings by furnishing an efficient low-rank approximation to  $\hat{V}_{xx}$  that eliminates unnecessary full-rank evaluations of the action during the iterative SCF procedure (Sec. II C). This is followed by a detailed description of how these three theoretical and algorithmic advances are combined and seamlessly integrated into SeA (SCDM+exx+ACE)—a robust, accurate, and computationally efficient framework for high-throughput condensed-phase hybrid DFT for large-scale finite-gap systems (Sec. II D).

### A. SCDM: A Robust and Non-Iterative Orbital Localization Scheme

To generate the localized orbitals needed for exx, SeA employs the selected columns of the density matrix (SCDM) approach,<sup>35</sup> a robust and non-iterative al-

ternative to the well-known MLWF procedure<sup>50,51</sup> used throughout the development of `exx`.<sup>26,33,47,49</sup> Since this work focuses on EXX calculations involving large-scale finite-gap systems, we will center our discussion around the  $\Gamma$ -point specific SCDM algorithm.<sup>35</sup> However, this choice is not an intrinsic limitation of the `SeA` approach, as `exx` could (in principle) utilize localized orbitals obtained via Brillouin zone sampling of the canonical KS orbitals with the SCDM-k approach.<sup>65</sup> The theoretical foundation underlying the SCDM approach is the “nearsightedness” principle popularized by Kohn,<sup>66,67</sup> which states that the elements of the real-space one-particle density matrix ( $\mathbf{P}$ ), i.e.,  $P(\mathbf{r}, \mathbf{r}') = \langle \mathbf{r} | \hat{P} | \mathbf{r}' \rangle = \sum_i^{N_{\text{occ}}} \langle \mathbf{r} | \phi_i \rangle \langle \phi_i | \mathbf{r}' \rangle$ , are exponentially decaying with respect to  $|\mathbf{r} - \mathbf{r}'|$  in finite-gap systems. On a real-space mesh with  $N_{\text{grid}}$  points,  $\mathbf{P} = \Phi \Phi^T$  is thus an  $N_{\text{grid}} \times N_{\text{grid}}$  matrix constructed from  $\Phi$ , the corresponding  $N_{\text{grid}} \times N_{\text{occ}}$  wavefunction matrix with columns given by a set of  $N_{\text{occ}}$  orbitals which span the occupied space ( $\{\phi_i\}$ ), e.g., the canonical KS occupied orbitals. As such,  $\mathbf{P}$  is rank-deficient with a column space dimension of  $\text{Rank}(\mathbf{P}) = N_{\text{occ}}$ , from which one can obtain a localized representation of the occupied space by selecting (and orthogonalizing) a set of  $N_{\text{occ}}$  well-conditioned columns of  $\mathbf{P}$ .

In the SCDM approach, this set of columns is obtained from a column-pivoted QR factorization of the  $N_{\text{occ}} \times N_{\text{grid}}$   $\Phi^T$  matrix (instead of the significantly larger  $\mathbf{P}$  matrix), as this alternative formulation yields equivalent column selection at significantly lower computational cost.<sup>35</sup> Performing this factorization yields:

$$\Phi^T \Pi = \mathbf{Q} \mathbf{R}, \quad (1)$$

in which  $\Pi$  is the  $N_{\text{grid}} \times N_{\text{grid}}$  permutation matrix (i.e., a dense representation of the selected column indices),  $\mathbf{Q}$  is an  $N_{\text{occ}} \times N_{\text{occ}}$  orthogonal matrix, and  $\mathbf{R}$  is an  $N_{\text{occ}} \times N_{\text{grid}}$  upper triangular matrix. The proto-SCDM orbitals (i.e., a well-conditioned set of localized but non-orthogonal orbitals that span the occupied space) are then given by the following  $N_{\text{grid}} \times N_{\text{occ}}$  matrix:

$$\mathbf{X} \equiv \mathbf{P}_{:,C} = \Phi(\Phi^T)_{:,C}, \quad (2)$$

in which “:” denotes all row indices,  $C$  is the set of indices corresponding to the  $N_{\text{occ}}$  selected columns, and  $(\Phi^T)_{:,C}$  is an  $N_{\text{occ}} \times N_{\text{occ}}$  matrix containing the first  $N_{\text{occ}}$  columns of  $\Phi^T \Pi$ . The final SCDM orbitals are then obtained via symmetric orthogonalization of the proto-SCDM orbitals, namely,

$$\tilde{\Phi} = \mathbf{X}(\mathbf{P}_{C,C})^{-1/2}, \quad (3)$$

in which  $\mathbf{P}_{C,C} = \mathbf{X}^T \mathbf{X}$  is the  $N_{\text{occ}} \times N_{\text{occ}}$  overlap matrix in the proto-SCDM basis (which is also equivalent to the density matrix in the basis selected by  $C$ ). In this expression, we follow the convention used during the development of `exx`:<sup>47,49</sup> all quantities that depend on the choice of localized orbitals (i.e., MLWFs in previous work

and SCDM in this work) are dressed with tildes, while all quantities invariant to the underlying orbital representation (e.g.,  $E_{\text{xx}}$ ) are left unmodified. By plugging Eq. (2) into Eq. (3), one can see that the input orbitals ( $\Phi$ ) are connected to the localized SCDM orbitals ( $\tilde{\Phi}$ ) via:

$$\tilde{\Phi} = \Phi(\Phi^T)_{:,C}(\mathbf{P}_{C,C})^{-1/2} \equiv \Phi \mathbf{U}, \quad (4)$$

in which

$$\mathbf{U} \equiv (\Phi^T)_{:,C}(\mathbf{P}_{C,C})^{-1/2} \quad (5)$$

is an  $N_{\text{occ}} \times N_{\text{occ}}$  unitary matrix that allows one to transform between these orbital representations by a single matrix multiplication. Hence, the non-iterative SCDM orbital localization scheme is able to furnish  $\mathbf{U}$  without the need for system-dependent optimization protocols, which makes it well-suited to provide the localized orbitals required by `exx` in the high-throughput `SeA` framework.

### B. `exx`: A Black-Box Linear-Scaling Exact-Exchange Algorithm for Finite-Gap Systems

With the completion of the non-iterative SCDM localization procedure, one can now perform the following unitary transformation (using  $\mathbf{U}$  from Eq. (5)),

$$\tilde{\phi}_i(\mathbf{r}) = \sum_j \phi_j(\mathbf{r})(\mathbf{U})_{ji}, \quad (6)$$

to obtain a set of localized orbitals that spans the occupied space and forms a basis for a computationally efficient linear-scaling evaluation of all EXX-related quantities needed during hybrid DFT calculations on large-scale finite-gap systems at the  $\Gamma$ -point. This is most easily illustrated by considering the canonical expression for  $E_{\text{xx}}$  (shown here for a closed-shell system for simplicity),

$$E_{\text{xx}} = - \sum_{ij} \int_{\Omega} \rho_{ij}(\mathbf{r}) v_{ij}(\mathbf{r}) d\mathbf{r}, \quad (7)$$

in which the sum includes all pairs of occupied orbitals, the integral is over the entire real-space domain in the periodic unit cell ( $\Omega$ ),  $\rho_{ij}(\mathbf{r}) \equiv \phi_i(\mathbf{r})\phi_j(\mathbf{r})$  is the orbital-product density, and  $v_{ij}(\mathbf{r})$  is the corresponding orbital-product potential (i.e., the solution to Poisson’s equation,  $\nabla^2 v_{ij}(\mathbf{r}) = -4\pi\rho_{ij}(\mathbf{r})$ ). In typical plane-wave/pseudopotential codes, this expression is evaluated with cubic-scaling cost using the conventional convolution-based EXX algorithm,<sup>20</sup> which performs a series of fast Fourier transforms (each scaling as  $\mathcal{O}(N_{\text{FFT}} \log N_{\text{FFT}})$ ) for each of the  $N_{\text{occ}}(N_{\text{occ}} + 1)/2$  unique pairs of occupied orbitals; see Fig. 2 for a schematic illustration of `vexx`, a working implementation of this approach in the PWSCF module of `QE`.<sup>52</sup> The fact that this expression is invariant to the unitary transformation in Eq. (6) forms the theoretical foundation for

the `exx` algorithm<sup>47,49</sup> (also in QE), which utilizes a basis of localized orbitals (MLWFs in previous work and SCDM in the current work) to exploit the following two levels of sparsity during the real-space evaluation of  $E_{\text{xx}}$ :

- *Pair selection*: only spatially overlapping orbitals need to be included when evaluating Eq. (7) in a localized basis; since each localized orbital has compact support and will only overlap with a constant number of neighboring orbitals, exploiting this level of sparsity reduces the total number of orbital pairs from quadratic to linear (i.e.,  $\sum_{ij} \rightarrow \sum_{\langle ij \rangle}$ ).
- *Domain truncation*: for each overlapping  $\langle ij \rangle$  pair, the spatial integral in Eq. (7) only needs to be evaluated on a domain which encompasses  $\tilde{\rho}_{ij}(\mathbf{r}) \equiv \tilde{\phi}_i(\mathbf{r})\tilde{\phi}_j(\mathbf{r})$ ; hence, this integral can be performed on orbital-pair-specific domains that are independent of the system size (i.e.,  $\int_{\Omega} \rightarrow \int_{\Omega_{ij}}$ ).

By harnessing these two levels of computational savings, `exx` enables an efficient linear-scaling evaluation of Eq. (7), which can now be rewritten in the following working form:

$$E_{\text{xx}} = - \sum_{\langle ij \rangle} \int_{\Omega_{ij}} \tilde{\rho}_{ij}(\mathbf{r}) \tilde{v}_{ij}(\mathbf{r}) d\mathbf{r}, \quad (8)$$

in which  $\tilde{\rho}_{ij}(\mathbf{r})$  and  $\tilde{v}_{ij}(\mathbf{r})$  are the orbital-product density and potential in the localized representation. After determining the set of overlapping pairs, `exx` computes  $\tilde{v}_{ij}(\mathbf{r})$  for a given  $\langle ij \rangle$  pair via the iterative (conjugate gradient) solution to Poisson's equation (PE),

$$\nabla^2 \tilde{v}_{ij}(\mathbf{r}) = -4\pi \tilde{\rho}_{ij}(\mathbf{r}) \quad \mathbf{r} \in \Omega_{ij}, \quad (9)$$

in the near-field region (i.e., for  $\mathbf{r} \in \Omega_{ij}$ ), in conjunction with boundary conditions provided by a sufficiently converged multipole expansion (ME):

$$\tilde{v}_{ij}(\mathbf{r}) = 4\pi \sum_{lm} \frac{Q_{lm}}{(2l+1)} \frac{Y_{lm}(\theta, \varphi)}{r^{l+1}} \quad \mathbf{r} \in \partial\Omega_{ij}. \quad (10)$$

In this expression,  $Y_{lm}(\theta, \varphi)$  are the spherical harmonics and  $Q_{lm}$  are the multipole moments associated with  $\tilde{\rho}_{ij}(\mathbf{r})$ , i.e.,

$$Q_{lm} = \int_{\Omega_{ij}} Y_{lm}^*(\theta, \varphi) r^l \tilde{\rho}_{ij}(\mathbf{r}) d\mathbf{r}. \quad (11)$$

In addition to the EXX contribution to the energy, hybrid DFT calculations also require evaluation of:

$$D_{\text{xx}}^i(\mathbf{r}) \equiv - \left( \frac{\delta E_{\text{xx}}}{\delta \phi_i^*(\mathbf{r})} \right) = -\hat{V}_{\text{xx}} \phi_i(\mathbf{r}), \quad (12)$$

a quantity that is often referred to as the EXX contribution to the wavefunction forces in the AIMD community, as it is needed to propagate the CPMD equations of motion. Of particular relevance to this work is the fact that

$D_{\text{xx}}^i(\mathbf{r})$  is also equivalent (to within a sign) to the action of the EXX operator ( $\hat{V}_{\text{xx}}$ ) on the (proto-)KS orbitals, a quantity that is needed to construct the xc potential during SCF calculations at the hybrid DFT level. While the evaluation of the canonical expression for  $D_{\text{xx}}^i(\mathbf{r})$  (shown here for a closed-shell system, cf. Eq. (7)),

$$D_{\text{xx}}^i(\mathbf{r}) = \sum_j v_{ij}(\mathbf{r}) \phi_j(\mathbf{r}) \quad \mathbf{r} \in \Omega, \quad (13)$$

is typically the computational bottleneck during the iterative SCF procedure, this quantity can also be efficiently computed in `exx` (analogous to  $E_{\text{xx}}$  above) by exploiting the two levels of sparsity inherent to a localized basis (i.e., pair selection and domain truncation). Since each localized orbital has compact support in real space, the sum over all orbitals in Eq. (13) can again be replaced by a sum over overlapping orbitals only ( $\sum_j \rightarrow \sum_{j \in \langle ij \rangle}$ ) with each contribution only needing to be evaluated on an orbital-specific (and system-size-independent) domain that encompasses  $\tilde{\phi}_j(\mathbf{r})$  (i.e.,  $\Omega \rightarrow \Omega_{ij}^D$ ). By harnessing these two levels of computational savings, `exx` enables an efficient linear-scaling evaluation of Eq. (13), which can now be rewritten in the following working form:

$$\tilde{D}_{\text{xx}}^i(\mathbf{r}) = \sum_{j \in \langle ij \rangle} \tilde{v}_{ij}(\mathbf{r}) \tilde{\phi}_j(\mathbf{r}) \quad \mathbf{r} \in \Omega_{ij}^D, \quad (14)$$

in which  $\tilde{v}_{ij}(\mathbf{r})$  in the near-field region (for  $\mathbf{r} \in \Omega_{ij}$ ) is provided by the solution to the PE in Eq. (9), while  $\tilde{v}_{ij}(\mathbf{r})$  in the far-field region (for  $\mathbf{r} \in \Omega_{ij}^D \setminus \Omega_{ij}$ ) is provided by the ME in Eq. (10). Unlike  $E_{\text{xx}}$ ,  $\tilde{D}_{\text{xx}}^i(\mathbf{r})$  is not invariant to the underlying orbital representation and is therefore dressed with a tilde (following the convention used non-invariant quantities in Refs. 47 and 49). However, the canonical form of this quantity is straightforwardly obtained via the following unitary transformation (cf. Eq. (6)):

$$D_{\text{xx}}^i(\mathbf{r}) = \sum_j \tilde{D}_{\text{xx}}^j(\mathbf{r}) (\mathbf{U}^{-1})_{ji}, \quad (15)$$

in conjunction with the  $\mathbf{U}$  provided by the orbital localization scheme (MLWFs in previous work and SCDM in the current work). Here, we note that this transformation is also of particular relevance to this work as it allows the linear-scaling `exx` algorithm to directly attack the computational bottleneck which prohibits the routine use of hybrid DFT in applications involving large-scale condensed-phase systems—the central idea in the high-throughput SeA framework developed herein (see Sec. IID).

With a massively parallel hybrid MPI/OpenMP implementation<sup>47,49</sup> in the CP module of QE<sup>52</sup> (in conjunction with on-the-fly MLWF localization<sup>53</sup>), `exx` has enabled hybrid DFT based AIMD/CPMD simulations of large-scale condensed-phase systems containing 500–1000 atoms in the  $NVE/NVT$  and  $NpH/NpT$  en-

sembles with a wall time cost that is comparable to GGA-based KS-DFT,<sup>47,49</sup> and has been used to perform a number of challenging theoretical applications to date.<sup>33,54–60</sup> However, the direct use of this version of `exx` would not meet the *implicit* robustness requirements of a high-throughput framework (i.e., black-box/automatable algorithms), since this implementation relies on a set of system-dependent parameters to harness the two levels of computational savings described above (i.e., a pair distance cutoff ( $R_{\text{pair}}$ ) for pair selection; PE radii ( $R_{\text{PE}}^{\text{s}}$  and  $R_{\text{PE}}^{\text{ns}}$ ) and ME radii ( $R_{\text{ME}}^{\text{s}}$  and  $R_{\text{ME}}^{\text{ns}}$ ) for domain truncation, see Refs. 47 and 49 for more details). To address this issue, we now describe a recent extension<sup>62</sup> of `exx` that has replaced all of these parameters with a single system-*independent* orbital coverage threshold ( $\epsilon$ ). In this extension,  $\epsilon \ll 1$  is a physically motivated (and systematically improvable) tolerance used to construct the real-space domain  $\Omega_{ii} \subset \Omega$  that encompasses each  $\tilde{\rho}_{ii}(\mathbf{r})$  based on the following orbital normalization condition,

$$\int_{\Omega_{ii}} |\tilde{\phi}_i(\mathbf{r})|^2 d\mathbf{r} = \int_{\Omega_{ii}} \tilde{\rho}_{ii}(\mathbf{r}) d\mathbf{r} \geq 1 - \epsilon, \quad (16)$$

and therefore provides an *a priori* determination<sup>34,62</sup> of the accuracy in  $E_{\text{xx}}$  and  $\{\tilde{D}_{\text{xx}}^i(\mathbf{r})\}$  (or equivalently  $\{D_{\text{xx}}^i(\mathbf{r})\}$ ) computed using this approach. In practice, each  $\Omega_{ii}$  is represented by a tight axis-aligned bounding box (AABB)—a parallelepiped that accounts for the anisotropy in the shape and extent of each localized orbital, and provides a natural framework for *simultaneously* and *consistently* exploiting the two levels of sparsity described above. To do so, `exx` first identifies a set of proto- $\langle ij \rangle$  pairs and corresponding orbital-pair-specific domains by finding all  $ij$  pairs with  $\Omega_{ij} \equiv \Omega_{ii} \cap \Omega_{jj} \neq \emptyset$ . To arrive at the final (and significantly smaller) set of  $\langle ij \rangle$  pairs, `exx` then screens the proto- $\langle ij \rangle$  pairs according to the following (absolute) orbital overlap criterion:

$$S_{[i,j]} \equiv \int_{\Omega_{ij}} |\tilde{\phi}_i(\mathbf{r})\tilde{\phi}_j(\mathbf{r})| d\mathbf{r} = \int_{\Omega_{ij}} |\tilde{\rho}_{ij}(\mathbf{r})| d\mathbf{r} \geq \delta. \quad (17)$$

In this expression,  $\delta > 0$  is automatically determined in `exx` to balance the errors made when computing the self ( $\langle ii \rangle$ ) contributions to  $E_{\text{xx}}$  (governed by  $\epsilon$  only) and non-self ( $\langle ij \rangle$ ) contributions to  $E_{\text{xx}}$  (governed by  $\epsilon$  and  $\delta$ ).<sup>62</sup> We note in passing that the use of an absolute orbital overlap criterion in `exx` was inspired by Refs. 43 and 44; however, the integral in Eq. (17) is restricted to  $\Omega_{ij}$  in `exx` (instead of the entire real-space domain  $\Omega$ ), which leads to a linear-scaling pair-selection protocol. Following the detailed derivation provided in Ref. 62,  $\Omega_{ij}^D$  was set to  $\text{scale}_{2\times} \Omega_{ii}$  (for  $j = i$ ) and  $\Omega_{jj}$  (for  $j \neq i$ ) when computing  $\{\tilde{D}_{\text{xx}}^i(\mathbf{r})\}$  via Eq. (14), which yields an accurate and efficient linear-scaling evaluation of these mission-critical terms. As described in Ref. 62, this version of `exx` is quite robust and able to treat both homogeneous and heterogeneous (i.e., multi-phase and/or multi-component) systems with controllable (and *a priori*

determined) accuracy and markedly improved computational efficiency, thereby making it well-suited to be the core EXX engine in the high-throughput SeA framework.

### C. ACE: An Efficient Low-Rank Approximation to the Exact-Exchange Operator

While the combined use of SCDM and this recently extended version of `exx` already provides a robust, accurate, and efficient core EXX engine for high-throughput hybrid DFT calculations of large-scale finite-gap systems, there is a third level of computational savings (independent from the two levels provided by SCDM+`exx`) that could be harnessed to further increase the efficiency of the SCF procedure at this level of theory. As pointed out by Lin,<sup>36</sup> the most computationally demanding steps during the iterative solution to the KS-DFT equations at the hybrid level—the repeated evaluation of the action using the standard/full-rank EXX operator (e.g.,  $\hat{V}_{\text{xx}}\phi_i$  in Eqs. (12)–(13))—can be completely replaced with significantly more efficient evaluations of this term using a low-rank approximation for  $\hat{V}_{\text{xx}}$  (i.e., the adaptively compressed exchange (ACE) operator,  $\hat{V}_{\text{xx}}^{\text{ACE}}$ ). As outlined in Algorithm 1, the ACE approach exploits the double-loop SCF structure quite commonly used when performing hybrid DFT calculations in condensed-phase electronic structure packages like QE. Although  $\hat{V}_{\text{xx}}^{\text{ACE}}$  can in prin-

---

#### Algorithm 1: SCF procedure with ACE

---

```

while  $\{|\phi_i\rangle\}$  not converged do
    ACE_Construction( $\{|\phi_i\rangle\}$ ;  $\hat{V}_{\text{xx}}^{\text{ACE}}$ );
     $\{|\chi_i\rangle\} \leftarrow \{|\phi_i\rangle\}$ ;
    while  $\{|\chi_i\rangle\}$  not converged do
         $\rho(\mathbf{r}) \leftarrow \sum_i |\chi_i(\mathbf{r})|^2$ ;
        SCF_Iteration( $\rho(\mathbf{r})$ ,  $\hat{V}_{\text{xx}}^{\text{ACE}}$ ;  $\{|\chi_i\rangle\}$ );
    end
     $\{|\phi_i\rangle\} \leftarrow \{|\chi_i\rangle\}$ ;
end

```

---

ciple be constructed from (and applied to) both occupied and virtual/unoccupied (proto-)KS orbitals,<sup>36</sup> we will limit our discussion below to the ACE procedure involving occupied (proto-)KS orbitals only; however, this choice is not an intrinsic limitation of the SeA approach, which could be extended to include virtual (proto-)KS orbitals as well.

During each outer-loop iteration, the ACE\_Construction function (i.e., the computational bottleneck for large-scale hybrid DFT calculations) takes in the set of proto-KS orbitals  $\{|\phi_i\rangle\}$  and performs a full-rank evaluation of the action to obtain  $\{D_{\text{xx}}^i\}$  via  $|D_{\text{xx}}^i\rangle = -\hat{V}_{\text{xx}}|\phi_i\rangle$ . In this section, we use bra-ket notation to emphasize the fact that the ACE approach is independent of the underlying representation; in other words, one has the flexibility to work in real and/or reciprocal space (i.e., using

$D_{xx}^i(\mathbf{r}) = \langle \mathbf{r} | D_{xx}^i \rangle$  and/or  $D_{xx}^i(\mathbf{G}) = \langle \mathbf{G} | D_{xx}^i \rangle$ . The output of `ACE_Construction` is the ACE operator:

$$\hat{V}_{xx}^{\text{ACE}} = - \sum_k |\xi_k\rangle \langle \xi_k|, \quad (18)$$

a low-rank approximation of  $\hat{V}_{xx}$  that is obtained via a Cholesky decomposition of the  $N_{\text{occ}} \times N_{\text{occ}}$  symmetric positive semi-definite matrix  $M_{ij} \equiv \langle \phi_i | D_{xx}^j \rangle = (\mathbf{L}\mathbf{L}^T)_{ij}$  to yield  $|\xi_k\rangle \equiv -\sum_i |D_{xx}^i\rangle (\mathbf{L}^{-T})_{ik}$  for  $k = 1, \dots, N_{\text{occ}}$ . Here, we note that the use of  $|D_{xx}^i\rangle$  instead of  $\hat{V}_{xx}|\phi_i\rangle$  leads to a sign difference in  $M_{ij}$  when compared to the original formulation.<sup>36</sup>

With the completion of the `ACE_Construction` step, a set of auxiliary orbitals,  $\{|\chi_i\rangle\}$ , is initialized to the current set of proto-KS orbitals (i.e.,  $\{|\chi_i\rangle\} \leftarrow \{|\phi_i\rangle\}$ ) as one enters the inner-loop. Inside the inner-loop, the KS-DFT equations are iteratively solved with a series of calls to the `SCF_Iteration` function, which takes  $\rho(\mathbf{r}) = \sum_i |\chi_i(\mathbf{r})|^2$  (the charge density in real space) and  $\hat{V}_{xx}^{\text{ACE}}$  as input. During each `SCF_Iteration` call,  $\rho(\mathbf{r})$  is used to construct the semi-local (non-EXX) contribution to the KS Hamiltonian and  $\hat{V}_{xx}^{\text{ACE}}|\chi_i\rangle$  (evaluated with the *fixed*  $\hat{V}_{xx}^{\text{ACE}}$  operator) is used to compute the EXX action. Throughout the inner-loop iterations,  $\{|\chi_i\rangle\}$  and the semi-local contributions to the KS Hamiltonian are updated towards self-consistency, while  $\hat{V}_{xx}^{\text{ACE}}$  remains fixed/unmodified. Upon convergence, the proto-KS orbitals are updated (i.e.,  $\{|\phi_i\rangle\} \leftarrow \{|\chi_i\rangle\}$ ) for the next outer-loop iteration.

The ACE algorithm is completed once the proto-KS orbitals reach self-consistency, i.e., a fully self-consistent hybrid DFT calculation. At this point,  $\hat{V}_{xx}^{\text{ACE}}$  reproduces the action of  $\hat{V}_{xx}$  on the occupied KS orbitals, and the EXX energy can be conveniently evaluated via (shown here for a closed-shell system at the  $\Gamma$ -point for consistency with Eqs. (7) and (12)):

$$E_{xx} = \sum_i \langle \phi_i | \hat{V}_{xx}^{\text{ACE}} | \phi_i \rangle = - \sum_{ik} |\langle \phi_i | \xi_k \rangle|^2, \quad (19)$$

in which each sum is over the converged occupied KS orbitals. In doing so, the ACE approach offers an additional level of computational savings (in addition to the two provided by `SCDM+exx`) that can be harnessed during the iterative solution to the KS-DFT equations at the hybrid level, thereby making it well-suited to further improve the efficiency of the high-throughput SeA framework.

#### D. SeA (SCDM+exx+ACE): High-Throughput Hybrid DFT for Large-Scale Finite-Gap Systems

In this section, we describe how SeA combines and seamlessly integrates SCDM, `exx`, and ACE into a robust, accurate, and computationally efficient framework for performing high-throughput condensed-phase hybrid

DFT calculations on large-scale finite-gap systems. For a robust, accurate, and efficient evaluation of the action using the standard/full-rank EXX operator ( $\hat{V}_{xx}|\phi_i\rangle$ )—the typical bottleneck during SCF calculations at the hybrid DFT level—SeA employs the non-iterative SCDM procedure for localized orbital generation described in Sec. II A in conjunction with the recently extended black-box version<sup>62</sup> of `exx` described in Sec. II B. To further improve the overall efficiency, SeA also employs the ACE operator formalism described in Sec. II C to reduce the number of times that  $|D_{xx}^i\rangle = -\hat{V}_{xx}|\phi_i\rangle$  needs to be evaluated during the iterative solution to the KS-DFT equations. In doing so, SeA harnesses three distinct levels of computational savings by reducing the number of calls to the most computational demanding step in hybrid DFT calculations (ACE, one level of savings), but also drastically reducing the cost of evaluating each of the remaining calls (SCDM+`exx`, two levels of savings). As mentioned above, SeA was inspired by the work of Dawson and Gygi,<sup>34</sup> Giannozzi and coworkers,<sup>43</sup> and Nair and coworkers,<sup>44,45</sup> and differs from this pioneering work (which harnessed one or two levels of computational savings via pair selection and ACE) by harnessing three levels of savings (pair selection, domain truncation, and ACE) to further enable the routine use of hybrid DFT in high-throughput applications involving large-scale finite-gap systems.

More specifically, SeA effectively involves a key modification to the ACE approach, which already offers tremendous speedups during hybrid DFT calculations by replacing the repeated evaluation of  $\hat{V}_{xx}|\phi_i\rangle$  in the iterative SCF procedure with significantly more efficient evaluations of this term using  $\hat{V}_{xx}^{\text{ACE}}$ . In the ACE-based SCF procedure depicted in Algorithm 1, the construction of  $\hat{V}_{xx}^{\text{ACE}}$  operator is the computational bottleneck (particularly for large-scale systems) and is accomplished via calls to the `ACE_Construction` function during each outer-loop iteration. To eliminate this step as the computational bottleneck during such large-scale hybrid DFT calculations, SeA directly attacks the cost of executing the `ACE_Construction` function by using SCDM+`exx` to compute  $|D_{xx}^i\rangle = -\hat{V}_{xx}|\phi_i\rangle$ . To illustrate the combination and seamless integration of these methods in more detail, we will focus the remainder of this discussion on a  $\Gamma$ -point specific algorithm (i.e., as the target application of SeA is high-throughput hybrid DFT calculations on large-scale systems); a more general extension of SeA based on Brillouin zone sampling will be discussed in future work. As mentioned above in Sec. II C, we will also limit our discussion to the ACE procedure involving occupied (proto-)KS orbitals only; an extension of SeA to include virtual/unoccupied orbitals will also be discussed in future work.

To start, we first consider the `ACE_Construction` procedure in the convolution-based ACE algorithm in the PWSCF module of QE, which will be referred to as PWSCF (ACE) throughout the remainder of this work. In PWSCF (ACE), the `ACE_Construction` step (as illustrated in Fig. 2) includes a full-rank EXX evaluation



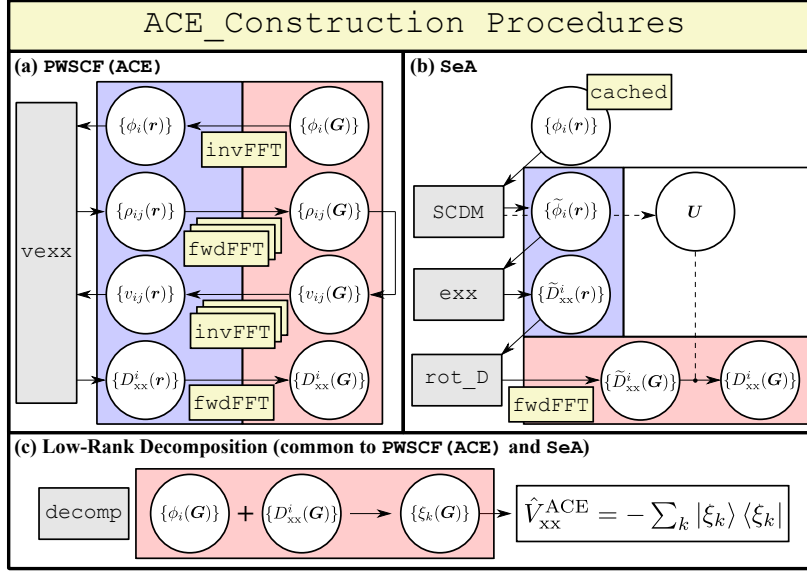


FIG. 2. Schematic illustration of the ACE\_Construction procedure in: (a) PWSCF (ACE), the convolution-based ACE implementation in PWSCF, (b) SeA, the high-throughput hybrid DFT framework presented in this work, and (c) the low-rank decomposition step common to (a) and (b). Starting from the (proto-)KS orbitals (either the stored  $\{\phi_i(\mathbf{G})\}$  in reciprocal space or cached  $\{\phi_i(\mathbf{r})\}$  in real space), both PWSCF (ACE) and SeA proceed to compute  $D_{xx}^i(\mathbf{G}) = -\hat{V}_{xx}\phi_i(\mathbf{G}) \forall i$  (i.e., the action of the full-rank EXX operator needed during the iterative SCF procedure in hybrid DFT calculations). Then, both algorithms merge at a common low-rank decomposition step that builds  $\hat{V}_{xx}^{\text{ACE}}$  from  $\{D_{xx}^i(\mathbf{G})\}$  and the stored  $\{\phi_i(\mathbf{G})\}$ . Pale blue (red) backgrounds indicate the real-space (reciprocal-space) aspects of each algorithm. Single yellow boxes (with fwdFFT or invFFT enclosed) depict a linear ( $\mathcal{O}(N_{\text{occ}})$ ) number of FFT calls, while triplets of such boxes represent a quadratic ( $\mathcal{O}(N_{\text{occ}}^2)$ ) number of FFT calls. For more details, a pedagogical walk-through of the ACE\_Construction procedure is provided in Sec. II D.

to obtain  $\{D_{xx}^i(\mathbf{G})\}$  (via the `vexx` function, Fig. 2(a)) followed by a low-rank decomposition to obtain  $\hat{V}_{xx}^{\text{ACE}}$  (via the `decomp` function, Fig. 2(c)). During a  $\Gamma$ -point calculation, `vexx` first obtains the (proto-)KS orbitals in real space ( $\{\phi_i(\mathbf{r})\}$ ) from their stored  $N_{\text{pw}}$  plane-wave coefficients ( $\{\phi_i(\mathbf{G})\}$ ) via the inverse FFT (`invFFT`). The complete set of orbital-product densities  $\{\rho_{ij}(\mathbf{r})\}$  is then constructed (as products over the  $N_{\text{occ}}(N_{\text{occ}} + 1)/2$  unique pairs of  $\phi_i(\mathbf{r})$ ) and converted to reciprocal space ( $\{\rho_{ij}(\mathbf{r})\} \rightarrow \{\rho_{ij}(\mathbf{G})\}$ ) using the forward FFT (`fwdFFT`). Based on the convolution theorem, the corresponding orbital-product potentials are evaluated as  $v_{ij}(\mathbf{G}) = 4\pi\rho_{ij}(\mathbf{G})/|\mathbf{G}|^2$ , which is again brought back to real space via the `invFFT` to form  $\{v_{ij}(\mathbf{r})\}$ . Then,  $\{D_{xx}^i(\mathbf{r})\}$  is formed in real space via  $D_{xx}^i(\mathbf{r}) = \sum_j v_{ij}(\mathbf{r})\phi_j(\mathbf{r})$  as described in Eq. (13) and converted to the targeted  $\{D_{xx}^i(\mathbf{G})\}$  via the `fwdFFT`. Hence, the cost of `vexx` is primarily governed by the two FFT operations involving  $\{\rho_{ij}\}$  and  $\{v_{ij}\}$  (each of which scales as  $\mathcal{O}(N_{\text{FFT}} \log N_{\text{FFT}})$ ) for each of the  $\mathcal{O}(N_{\text{occ}}^2)$  unique pairs of occupied orbitals, which leads to an overall cubic scaling algorithm (i.e.,  $\mathcal{O}(N_{\text{occ}}^2 N_{\text{FFT}} \log N_{\text{FFT}})$ ) after neglecting the logarithmic term. After obtaining the targeted  $\{D_{xx}^i(\mathbf{G})\}$ , PWSCF (ACE) completes the ACE\_Construction step with a call to `decomp`, a function which constructs  $\hat{V}_{xx}^{\text{ACE}}$  via Eq. (18) using the stored  $\{\phi_i(\mathbf{G})\}$ . The procedure for constructing  $\hat{V}_{xx}^{\text{ACE}}$  is schematically illustrated in Fig. 2(c) (and covered in

more detail in Sec. II C), and also requires cubic scaling cost ( $\mathcal{O}(N_{\text{pw}} N_{\text{occ}}^2 + N_{\text{occ}}^3)$ ). To allow for lossless fwdFFT and invFFT, the number of (real-space) grid points ( $N_{\text{FFT}}$ ) is larger than  $N_{\text{pw}}$ ; hence, `vexx` generally dominates `decomp` and is (almost always) the computational bottleneck during the ACE\_Construction step in PWSCF (ACE).

To greatly improve the computational efficiency of hybrid DFT calculations (particularly for large-scale systems), SeA directly attacks this computational bottleneck in PWSCF (ACE) by replacing `vexx` with a procedure based on the combination of SCDM and `exx`. As depicted in Fig. 2(b), the ACE\_Construction procedure in SeA starts from the readily available real-space (proto-)KS orbitals  $\{\phi_i(\mathbf{r})\}$  (which are cached during the calculation of the total charge density needed by the underlying semi-local DFT<sup>47</sup> and provided on the real-space mesh with  $N_{\text{grid}} = N_{\text{FFT}}$  grid points). Then, SeA applies the non-iterative SCDM algorithm (i.e., by calling the SCDM function) to obtain the localized orbitals in real space  $\{\tilde{\phi}_i(\mathbf{r})\}$  and the corresponding unitary matrix  $\mathbf{U}$  that allows one to transform between the local and canonical orbital representations; as detailed in Sec. II A, execution of SCDM has a cubic scaling cost of  $\mathcal{O}(N_{\text{FFT}} N_{\text{occ}}^2 + N_{\text{occ}}^3)$ . With the localized SCDM orbitals in hand, SeA then calls the linear-scaling `exx` routine, which harness two levels of computational savings during the real-space evaluation of  $\{\tilde{D}_{xx}^i(\mathbf{r})\}$  via Eq. (14))



at  $\mathcal{O}(N_{\text{occ}})$  cost (see Sec. II B). In doing so, SeA replaces the computationally dominant FFT operations involving  $\{\rho_{ij}\}$  and  $\{v_{ij}\}$  in `vexx` with a non-iterative cubic-scaling localization routine and a linear-scaling evaluation of  $\{\tilde{D}_{\text{xx}}^i(\mathbf{r})\}$ . Here, we remind the reader that the recently extended version<sup>62</sup> of `exx` included in SeA is based on a single system-independent orbital coverage threshold (instead of the set of system-dependent parameters used in previous `exx` versions<sup>47,49</sup>), which allows for *a priori* tuning of the balance between accuracy and performance during this critical step in the `ACE_Construction` procedure. Then, SeA calls the `rot_D` function, which first transforms  $\{\tilde{D}_{\text{xx}}^i(\mathbf{r})\}$  to  $\{\tilde{D}_{\text{xx}}^i(\mathbf{G})\}$  via the `fwdFFT`; this step is the local representation analog of the  $\{D_{\text{xx}}^i(\mathbf{r})\} \xrightarrow{\text{fwdFFT}} \{D_{\text{xx}}^i(\mathbf{G})\}$  transformation in `vexx` and comes with an equivalent quadratic scaling cost of  $\mathcal{O}(N_{\text{occ}}N_{\text{FFT}}\log N_{\text{FFT}})$ , i.e., after neglecting the logarithmic term common to both transformations. To form the targeted  $\{D_{\text{xx}}^i(\mathbf{G})\}$ , `rot_D` then rotates  $\{\tilde{D}_{\text{xx}}^i(\mathbf{G})\}$  via:

$$D_{\text{xx}}^i(\mathbf{G}) = \sum_j \tilde{D}_{\text{xx}}^j(\mathbf{G})(U^{-1})_{ji}, \quad (20)$$

with a cubic scaling associated cost of  $\mathcal{O}(N_{\text{pw}}N_{\text{occ}}^2)$ . Here, we would emphasize that the availability of the unitary  $U$  matrix in SeA (provided by the earlier call to `SCDM`) greatly facilitates this transformation, leveraging a strategy previously pointed out by Nair and co-workers.<sup>44</sup> While the order in which the `fwdFFT` and the unitary rotation are applied leads to the same  $\{D_{\text{xx}}^i(\mathbf{G})\}$ , the order employed in `rot_D` is the more computationally efficient of the two. More specifically, the procedure in `rot_D` ( $\{\tilde{D}_{\text{xx}}^i(\mathbf{r})\} \xrightarrow{\text{fwdFFT}} \{\tilde{D}_{\text{xx}}^i(\mathbf{G})\} \xrightarrow{U^{-1}} \{D_{\text{xx}}^i(\mathbf{G})\}$ ) has an associated computational cost of  $\mathcal{O}(N_{\text{occ}}N_{\text{FFT}}\log N_{\text{FFT}} + N_{\text{pw}}N_{\text{occ}}^2)$ , while the alternative choice ( $\{\tilde{D}_{\text{xx}}^i(\mathbf{r})\} \xrightarrow{U^{-1}} \{D_{\text{xx}}^i(\mathbf{r})\} \xrightarrow{\text{fwdFFT}} \{D_{\text{xx}}^i(\mathbf{G})\}$ ) scales as  $\mathcal{O}(N_{\text{FFT}}N_{\text{occ}}^2 + N_{\text{occ}}N_{\text{FFT}}\log N_{\text{FFT}})$ . As such, the `rot_D` routine leverages the fact that  $N_{\text{FFT}} > N_{\text{pw}}$  for lossless `fwdFFT` and `invFFT` to further improve the efficiency of SeA. After obtaining the targeted  $\{D_{\text{xx}}^i(\mathbf{G})\}$ , SeA merges with `PWSCF(ACE)` by calling the common `decomp` function described above (Fig. 2(c)) to obtain  $\hat{V}_{\text{xx}}^{\text{ACE}}$  and complete the `ACE_Construction` procedure.

By constructing  $\hat{V}_{\text{xx}}^{\text{ACE}}$  in the canonical orbital representation (via  $\{\phi_i(\mathbf{G})\}$  and  $\{D_{\text{xx}}^i(\mathbf{G})\}$ ), the current version of SeA sidesteps the need to work with localized orbitals during the inner-loop iterations in Algorithm 1. While the use of localized orbitals could provide additional computational savings during the inner-loop iterations, such savings would need to be balanced against the cost associated with multiple calls to `SCDM`; hence, this potential future research direction is beyond the scope of this work. With  $\hat{V}_{\text{xx}}^{\text{ACE}}$  in hand (at the end of a given outer-loop iteration and/or SCF convergence), the current version of SeA computes  $E_{\text{xx}}$  via Eq. (19). Here, we

note that Eq. (8) (i.e., the real-space  $E_{\text{xx}}$  expression in the `exx` approach) is not used in SeA, as the real-space evaluation of this quantity in a planewave code such as `QE` would be subject to small (but non-negligible) errors (e.g., aliasing and domain truncation). Since  $\hat{V}_{\text{xx}}^{\text{ACE}}$  is independent of the underlying representation, it would also be possible to construct a fully real-space version of SeA (i.e., by eliminating the `fwdFFT` in `rot_D` and using  $\{\phi_i(\mathbf{r})\}$  and  $\{D_{\text{xx}}^i(\mathbf{r})\}$  to perform the low-rank decomposition in `decomp`). While a naïve implementation of such an approach in a planewave code would be subject to aliasing errors (which can impair very tight SCF convergence, e.g., as needed for numerical phonon calculations), the implementation of a fully real-space version of SeA in a real-space electronic structure code like `PARSEC`<sup>68</sup> has the potential to enable hybrid DFT calculations across significantly larger length- and time-scales.

### III. ACCURACY AND PERFORMANCE OF SEA

In this section, we assess the accuracy and performance of SeA by comparing this approach against the convolution-based ACE implementation in `PWSCF` (cf. the SeA and `PWSCF(ACE)` algorithms in Fig. 2). The computational details for all electronic structure calculations performed in this work can be found in Appendix A. To do so, we carried out a series of fully self-consistent `PBE0`<sup>63,64</sup> calculations using SeA and `PWSCF(ACE)` for 200 randomly selected  $(\text{H}_2\text{O})_{64}$  configurations (each with a cubic unit cell) that were collected during active learning<sup>69,70</sup> of a deep neural network (DNN) potential for water at the SCAN meta-GGA level of theory<sup>71</sup>, which is known to perform quite well for aqueous systems.<sup>72–78</sup> This set contains a wide range of non-equilibrium configurations (including intact and auto-ionized water molecules) with densities ranging from  $\approx 0.5 \text{ g/cm}^3$  to  $\approx 1.5 \text{ g/cm}^3$ . While it is straightforward to apply SeA to significantly larger systems (*vide infra*), our choice to consider  $(\text{H}_2\text{O})_{64}$  here allows for a systematic comparison with the reference (and more computationally demanding) `PWSCF(ACE)` approach.

We begin by discussing the accuracy of SeA when computing converged  $E_{\text{xx}}$  values for these 200 non-equilibrium  $(\text{H}_2\text{O})_{64}$  configurations using the default ( $\epsilon = 10^{-4}$ ) setting in the `exx` function (i.e., the system-independent orbital coverage threshold<sup>62</sup> in Eq. (16)). As depicted in Fig. 3(a), we found that SeA consistently yields accurate  $E_{\text{xx}}$  values with median (maximum) absolute percent errors of  $5.2 \times 10^{-3}\%$  ( $1.1 \times 10^{-2}\%$ ). While there is no formal variational principle in SeA, we did observe that the EXX energies obtained using this approach (with  $\epsilon = 10^{-4}$ ) are variational for these aqueous systems, i.e., all of the SeA energy values are higher (more positive) than those obtained with `PWSCF(ACE)`. Here, we would argue that the remaining systematic error is largely due to pair truncation (i.e., the exclusion of orbital pairs with small but finite  $S_{|i,j|}$  values, cf. Eq. (17))

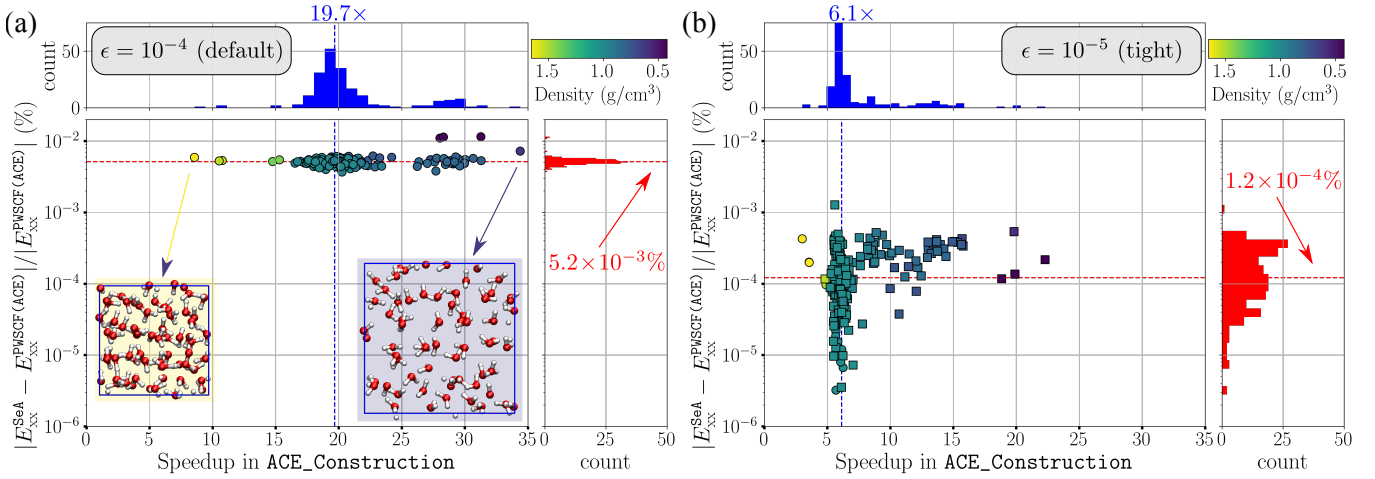


FIG. 3. Accuracy and performance of SeA (compared to the convolution-based PWSCF (ACE) implementation in QE) when computing  $E_{xx}$  for 200 non-equilibrium  $(\text{H}_2\text{O})_{64}$  configurations (which include intact and auto-ionized water molecules, with densities ranging from  $\approx 0.5 \text{ g/cm}^3$  to  $\approx 1.5 \text{ g/cm}^3$ ) using: **(a)** the default setting ( $\epsilon = 10^{-4}$ ) in `exx` and **(b)** a tighter setting ( $\epsilon = 10^{-5}$ ). In each panel, the central scatter plot shows the correlation between accuracy (which is quantified using the absolute percent error in the EXX energy computed with SeA,  $E_{xx}^{\text{SeA}}$ , compared to the PWSCF (ACE) reference,  $E_{xx}^{\text{PWSCF(ACE)}}$ ) and performance (which is quantified by the speedup observed in the wall time cost of the ACE\_Construction step, the typical bottleneck in PWSCF (ACE)). Closed circles (squares) in each scatter plot are colored according to the system density and represent variational (non-variational) errors in which  $E_{xx}^{\text{SeA}} \geq E_{xx}^{\text{PWSCF(ACE)}}$  ( $E_{xx}^{\text{SeA}} < E_{xx}^{\text{PWSCF(ACE)}}$ ). The histograms bordering each scatter plot depict the marginalized distributions corresponding to the accuracy (right border, red) and performance (top border, blue), with median values denoted by dashed lines. Each calculation was performed using the Cori-KNL architecture with one MPI process per node (and all 68 available physical cores per node used as core-bound OpenMP threads). The number of MPI processes was chosen to be equivalent to the number of real-space grid points along each lattice direction. See the main text for more details as well as a critical assessment of the ionic forces furnished by SeA.

and domain truncation (i.e., the slight underestimation of the multipole moments used to obtain the boundary conditions for the PE as well as the far-field potential via the ME, cf. Eqs. (9)–(11)) in `exx`. Quite interestingly, we also note that the error is essentially flat across this diverse set of non-equilibrium aqueous configurations, which provides strong evidence that the recently extended version<sup>62</sup> of `exx` incorporated into SeA is quite robust and able to operate at an *a priori* determined level of accuracy set by  $\epsilon$  (see Sec. II B). In the three low-density configurations exhibiting minor deviations in Fig. 3(a), we observed a non-negligible degree of long-range order in their structures (e.g., clustering due to the formation of small void spaces). In such cases, the number of overlapping  $\langle ij \rangle$  pairs (which are automatically determined by `exx`) can be slightly underestimated; as described in Ref. 62, this (albeit minor) issue can be rectified with the use of a more sophisticated model for  $\delta$  based on the orbital pair correlation function. As an additional assessment, we also considered the accuracy of the ionic forces obtained using SeA for this set of non-equilibrium aqueous configurations. When compared to PWSCF (ACE), we found that SeA consistently yields accurate ionic force components with a root-mean-square error (RMSE) of  $1.1 \times 10^{-4} \text{ Ha/Bohr}$  and a maximum error of  $5.5 \times 10^{-4} \text{ Ha/Bohr}$ , both of which are small relative to the typical convergence criterion ( $\approx 1.0 \times 10^{-3} \text{ Ha/Bohr}$ ) used during the structural

relaxation of condensed-phase systems. Hence, we expect that SeA will also reproduce the structure and dynamics of large-scale finite-gap systems with high fidelity.

When using a tighter ( $\epsilon = 10^{-5}$ ) setting in `exx`, we found that the median (maximum) absolute percent errors in the EXX energy values computed using SeA were  $1.2 \times 10^{-4}\%$  ( $1.3 \times 10^{-3}\%$ )—an order-of-magnitude smaller than those obtained above with the default ( $\epsilon = 10^{-4}$ ) setting. As depicted in Fig. 3(b), the use of this tighter setting largely removes the systematic error in SeA; since there is no variational guarantee in SeA, we now observe both variational and (slightly) non-variational EXX energy values. In this case, the remaining non-systematic/random error is largely due to the use of finite-accuracy thresholds when computing  $\tilde{v}_{ij}(\mathbf{r})$  in the near-field (e.g., the non-zero residual in the conjugate-gradient solution of the PE, cf. Eq. (9)) and far-field (e.g., the use of a maximum angular momentum value in the ME, cf. Eqs. (10) and (11)). Furthermore, the ionic force components furnished by SeA are also significantly improved (by  $\approx 3\times$ ) when using this tighter  $\epsilon$  setting, i.e., yielding an RMSE of  $3.0 \times 10^{-5} \text{ Ha/Bohr}$  and a maximum error of  $1.3 \times 10^{-4} \text{ Ha/Bohr}$  compared to PWSCF (ACE).

We now assess the computational performance of SeA by focusing on the wall time associated with the ACE\_Construction step—the typical bottleneck during PWSCF (ACE) calculations of large-scale systems (see

Sec. IID and Fig. 2). As shown in Fig. 3(a), we found that SeA has a median speedup of  $\approx 19.7\times$  when using the default ( $\epsilon = 10^{-4}$ ) setting, and is therefore able to furnish highly accurate energies and ionic forces at the hybrid DFT level at a significantly reduced computational cost compared to PWSCF (ACE). In doing so, we found that the least dense configurations yielded the greatest speedup in the ACE\_Construction step ( $\approx 30\times$ ), while the most dense configurations yielded the least speedup ( $\approx 10\times$ ), cf. Fig. 3(a) insets. Since the least dense systems will have the smallest number of overlapping  $\langle ij \rangle$  pairs as well as the smallest overlapping  $\Omega_{ij}$  domains, this result is not surprising and provides further evidence that the recently extended version<sup>62</sup> of `exx` incorporated into SeA is able to exploit the increased degree of sparsity present in systems with low densities. Here, we would remind the reader that one should only expect the performance of SeA to have a semi-systematic dependence on the system density, since the degree of sparsity is also affected by the structural details of the underlying ionic framework in each configuration. When even higher accuracy is needed (e.g.,  $\epsilon = 10^{-5}$ ), SeA is still very computationally efficient and provides a median speedup of  $\approx 6.1\times$  in the ACE\_Construction step; for several of the low-density configurations considered in this work, we observed order-of-magnitude speedups ( $\approx 20\times$ ) during the evaluation of this bottleneck in PWSCF (ACE).

Having assessed the accuracy and performance of SeA on 200 non-equilibrium aqueous configurations, we now assess the relative performance of SeA with respect to PWSCF (ACE) via a detailed analysis of the wall time cost associated with each approach. To do so, we performed a series of fully self-consistent PBE0 calculations using SeA and PWSCF (ACE) for 15  $(\text{H}_2\text{O})_{64}$  configurations that were collected during active learning<sup>69,70</sup> of a DNN potential for water at the SCAN level,<sup>71</sup> none of which were taken from the 200 configurations considered above. To eliminate unnecessary complications associated with varying levels of parallel FFT efficiency (which are largely inconsequential for assessing the performance of SeA with respect to PWSCF (ACE)), these 15  $(\text{H}_2\text{O})_{64}$  snapshots (each of which has a cubic unit cell) all have a fixed  $(150 \times 150 \times 150)$ -point discretization of the real-space grid and densities ranging from  $0.81 \text{ g/cm}^3$ – $0.87 \text{ g/cm}^3$ . Unlike the non-equilibrium aqueous configurations used to construct Fig. 3, we expect that the timings from these 15 (approximately isochoric) snapshots will result in nearly symmetric unimodal distributions, and thereby report sample means (instead of medians) in this analysis. As reported in Table I, each SCF calculation required 5 ACE\_Construction (outer-loop) steps and 13 SCF\_Iteration (inner-loop) steps on average (cf. Algorithm 1). When using PWSCF (ACE), the overall cost was dominated by the ACE\_Construction steps (comprising  $\approx 88.9\%$  of the total wall time cost), while the SCF\_Iteration steps comprised the remaining  $\approx 11.1\%$ . During the ACE\_Construction steps

TABLE I. Detailed timings breakdown for SCF calculations at the PBE0 level using PWSCF (ACE) and SeA (default  $\epsilon = 10^{-4}$  setting). All wall times were averaged over 15 uncorrelated  $(\text{H}_2\text{O})_{64}$  snapshots (each with a fixed  $(150 \times 150 \times 150)$ -point FFT grid). All calculations were performed using 150 Cori-KNL nodes (with one MPI process and 68 OpenMP threads per node) starting from converged orbitals at the PBE<sup>79</sup> level; the number of SCF iterations during these preliminary PBE calculations (which are typically included in the PWSCF output file) were excluded from the reported calls to the SCF\_Iteration function.

Approach*	Function		Time (s/call)	Calls	Relative Cost
PWSCF (ACE)	ACE_Construction	vexx	211	5	88.8%
		decomp	0.24	5	0.1%
	SCF_Iteration		10.2	13	11.1%
SeA ( $\epsilon = 10^{-4}$ )	ACE_Construction	SCDM	4.82	5	12.7%
		exx	5.63	5	14.9%
		rot_D	0.66	5	1.8%
		decomp	0.24	5	0.6%
	SCF_Iteration		10.2	13	70.0%

\*For a single representative  $(\text{H}_2\text{O})_{64}$  configuration, the total wall time needed by the conventional (non-ACE) convolution-based EXX implementation in PWSCF was 20,499 s, compared to 1,224 s ( $16.7\times$  speedup) in PWSCF (ACE) and 198 s ( $103.5\times$  speedup) in SeA.

in PWSCF (ACE), computation of the targeted  $\{D_{xx}^i(\mathbf{G})\}$  via the `vexx` function (Fig. 2(a)) accounted for the lion’s share of the cost (i.e.,  $\approx 88.8\%$  of the total  $\approx 88.9\%$ ) while the cost of constructing  $\hat{V}_{xx}^{\text{ACE}}$  via `decomp` (Fig. 2(c)) was largely negligible ( $\approx 0.1\%$  of the total  $\approx 88.9\%$ ). We note in passing that once  $\hat{V}_{xx}^{\text{ACE}}$  was constructed, the cost of applying this operator during each SCF\_Iteration step (i.e.,  $\{V_{xx}^{\text{ACE}}|\chi_i\}$ ) was negligible ( $\lesssim 0.6\%$  of the SCF\_Iteration cost) and was therefore not reported separately in Table I.

When using SeA with the default ( $\epsilon = 10^{-4}$ ) setting in `exx`, the overall cost is now dominated by the SCF\_Iteration steps ( $\approx 70.0\%$ ), while the ACE\_Construction steps comprise the remaining  $\approx 30.0\%$ . By harnessing three levels of computational savings, SeA has therefore displaced the cost-prohibitive ACE\_Construction steps as the computational bottleneck during hybrid DFT calculations of systems with sizes similar to (and beyond)  $(\text{H}_2\text{O})_{64}$ . When compared against the original 211.24 s/call in PWSCF (ACE), the ACE\_Construction steps in SeA (Figs. 2(b) and 2(c)) cost 11.35 s/call; this represents an order-of-magnitude ( $\approx 18.6\times$ ) speedup in this previously rate-determining step and an  $\approx 6.3\times$  speedup in the overall cost when performing such hybrid DFT calculations. For comparison, we also performed a fully self-consistent PBE0 calculation on a single representative  $(\text{H}_2\text{O})_{64}$  configuration using the conventional (non-ACE) convolution-based EXX implementation in PWSCF, and found that SeA provided a two-order-of-magnitude speedup ( $103.5\times$ ) in the total wall time (see Table I footnote).

This  $\approx 18.6\times$  speedup in the computational bottleneck ACE\_Construction steps is robust (i.e., comparable to the median speedup of  $19.7\times$  found above in Fig. 3(a)) and warrants further discussion, particularly when SeA is used to perform higher-accuracy hybrid DFT calculations on systems much larger than  $(\text{H}_2\text{O})_{64}$ . During the ACE\_Construction steps in SeA, there are two dominant contributions (4.82 s/call from our ScaLAPACK-based SCDM routine and 5.63 s/call from `exx`) and two minor contributions (0.66 s/call from `rot_D` and 0.24 s/call from `decomp`) for systems like  $(\text{H}_2\text{O})_{64}$ . Since the cost of SCDM is comparable to `exx` here and will grow more quickly (cubic) with system size than `exx` (linear), a more efficient SCDM localization algorithm will become critical when applying SeA to larger systems; as such, improvements to the performance of the SCDM routine in SeA are currently under active development in our group. While the cost associated with `rot_D` and `decomp` remain small compared to `exx` for  $(\text{H}_2\text{O})_{64}$ , both of these routines also scale cubically with system size (but with smaller prefactors than SCDM) and will therefore become more important for significantly larger systems. When repeating the same calculations in Table I using a tighter ( $\epsilon = 10^{-5}$ ) setting in `exx`, the wall time cost of `exx` increased from 5.63 s/call to 21.44 s/call, leading to the following partition of the total cost in SeA: 9.0% (SCDM), 40.0% (`exx`), 1.2% (`rot_D`), 0.4% (`decomp`), and 49.4% (SCF\_Iteration). Even at this higher-fidelity setting (which should serve almost all users’ needs), SeA provides an  $\approx 7.8\times$  speedup in the ACE\_Construction steps, essentially balancing the cost of the ACE\_Construction steps ( $\approx 50.6\%$ ) with that of the SCF\_Iteration steps ( $\approx 49.4\%$ ).

#### IV. PROOF-OF-PRINCIPLE HIGH-THROUGHPUT APPLICATION: TRAINING A HYBRID DFT BASED DNN MODEL FOR LIQUID WATER WITH SEA

As a proof-of-principle high-throughput application, we now demonstrate how SeA can be used to efficiently train a converged deep neural network (DNN) potential for ambient ( $T = 300$  K,  $p = 1$  Bar) liquid water at the PBE0<sup>63,64</sup> level via the deep potential molecular dynamics (DPMD) active-learning protocol of Car, E, and co-workers<sup>80,81</sup> (Sec. IV A). We then assess the accuracy of this SeA-trained DNN potential on an out-of-sample test set containing several elevated-temperature  $(\text{H}_2\text{O})_{512}$  snapshots in Sec. IV B, and showcase the capabilities of SeA by directly computing the (ground truth) ionic forces in these challenging systems containing  $> 1,500$  atoms.

#### A. Convergence and Precision of the Model

Having assessed the accuracy and performance of SeA on a diverse set of 200 non-equilibrium  $(\text{H}_2\text{O})_{64}$  configurations (which include both intact and auto-ionized water molecules, and densities spanning  $0.5 \text{ g/cm}^3$ – $1.5 \text{ g/cm}^3$ ) collected during the active learning of a DNN potential for water at the meta-GGA (SCAN) level,<sup>69,70</sup> we now proceed to label (i.e., compute energies and ionic forces for) all 8,610 configurations in this collection at the hybrid (PBE0) DFT level using SeA ( $\epsilon = 10^{-5}$ ); see Appendix A for computational details regarding the electronic structure calculations. Based on this initial data set, we then trained a DNN for ambient liquid water ( $T = 300$  K,  $p = 1$  Bar) following the DPMD active-learning procedure outlined in Refs.<sup>80,81</sup> (see Appendix B for training details). Hence, the progress of the active-learning protocol was monitored by the model deviation ( $\mathcal{E}$ ) in the ionic forces  $\{\mathbf{F}_I\}$ :

$$\mathcal{E} \equiv \max_I \sqrt{\langle |\mathbf{F}_I - \langle \mathbf{F}_I \rangle|^2 \rangle}, \quad (21)$$

in which the max function was taken over all ions  $I$ , and the ensemble averages (denoted by  $\langle \cdot \rangle$ ) were evaluated over four independently trained DNN models (i.e., trained using the same data but different initial random seeds) for each snapshot in a given trajectory. From this expression, one can see that  $\mathcal{E}$  is a precision-based criterion that is measured among equivalently trained DNN models; an accuracy-based assessment, in which the ionic forces from the final DNN model(s) are directly compared to the ground-truth PBE0 ionic forces will be provided in Sec. IV B. For the trajectory needed in Eq. (21), we performed a DPMD simulation (i.e., a classical MD simulation propagated using one of the trained DNN models as the underlying force field) in the  $NpT$  ensemble ( $T = 300$  K,  $p = 1$  Bar); see Appendix B for more details. When configurations with large model deviations (i.e.,  $\mathcal{E} > 2.0 \times 10^{-3}$  Ha/Bohr) were encountered, these configurations were relabeled with SeA and added to the training set for the next round of active learning (i.e., DPMD exploration and configuration selection/relabeling). The active-learning process was stopped when the 90-th percentile of the  $\mathcal{E}$  probability density function ( $P(\mathcal{E})$ ) was below  $1.0 \times 10^{-3}$  Ha/Bohr, a typical convergence criterion used during structural relaxation in condensed-phase systems.

Doing so leads to a total of two active-learning iterations across a total of 8,705  $(\text{H}_2\text{O})_{64}$  configurations (i.e., yielding 95 additional configurations not contained in the initial training set). As shown in Fig. 4, the final  $P(\mathcal{E})$  at  $T = 300$  K and  $p = 1$  Bar (i.e., the thermodynamic conditions used during training) meets the convergence criterion outlined above and therefore depicts a converged DNN potential for ambient liquid water at the PBE0 level. As an additional assessment of the precision in our SeA-trained DNN model, we also performed DPMD simulations (using the DNN poten-

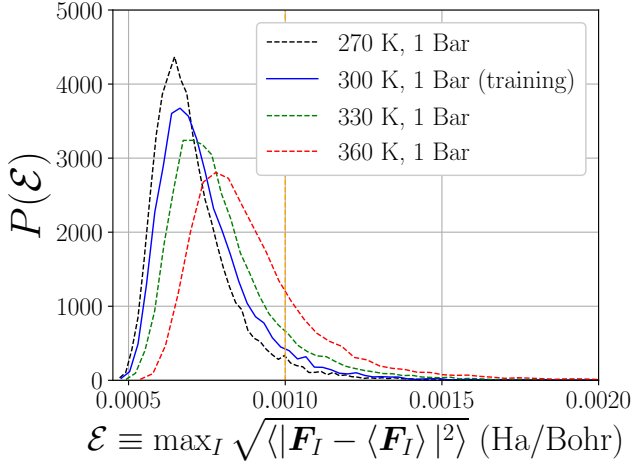


FIG. 4. Normalized probability density functions of the model deviation ( $\mathcal{E}$ ) in the ionic forces ( $\{\mathbf{F}_I\}$ ) over four independently trained DNN models of liquid water at  $T = 300$  K and  $p = 1$  Bar (solid blue line, training/active-learning thermodynamic condition) and  $T \in \{270 \text{ K}, 330 \text{ K}, 360 \text{ K}\}$  and  $p = 1$  Bar (dashed lines, out-of-sample thermodynamic conditions). In each case,  $\mathcal{E}$  was evaluated over a DPMD trajectory of  $(\text{H}_2\text{O})_{64}$  at the corresponding thermodynamic condition; ensemble averages were evaluated over the four DNN models and denoted by  $\langle \cdot \rangle$ . For comparison, a typical convergence criterion used during the structural relaxation of condensed-phase systems (i.e.,  $1.0 \times 10^{-3}$  Ha/Bohr) is depicted by the vertical orange line.

tial trained at  $T = 300$  K and 1 Bar) in the  $NpT$  ensemble at 270 K, 330 K, and 360 K. As expected, we find that  $\mathcal{E}$  tends to increase with  $T$  in Fig. 4, as the additional thermal energy causes the system to explore larger sectors of configuration space which were sampled less thoroughly by the active-learning process at 300 K. However, the trained DNN model still remains quite precise with relatively smooth/continuous  $P(\mathcal{E})$  distributions—the bulk of which are still below the desired  $10^{-3}$  Ha/Bohr threshold—even at such elevated temperatures. While  $P(\mathcal{E})$  can be further improved by performing additional active-learning steps, this is beyond the scope of this proof-of-principle high-throughput application, which illustrates the utility of SeA for training DNN potentials for large-scale finite-gap systems at the hybrid DFT level.

### B. Accuracy of the Model: Out-of-Sample Testing and a Beyond-One-Thousand-Atom Challenge

To assess the accuracy of this SeA-trained DNN model, we also compared its ionic force predictions against the ground truth (i.e., direct ionic force calculations at the hybrid (PBE0) DFT level using SeA with  $\epsilon = 10^{-5}$ ). As an initial assessment, we considered 16 equispaced  $(\text{H}_2\text{O})_{64}$  snapshots from the  $NpT$  DPMD simulation per-

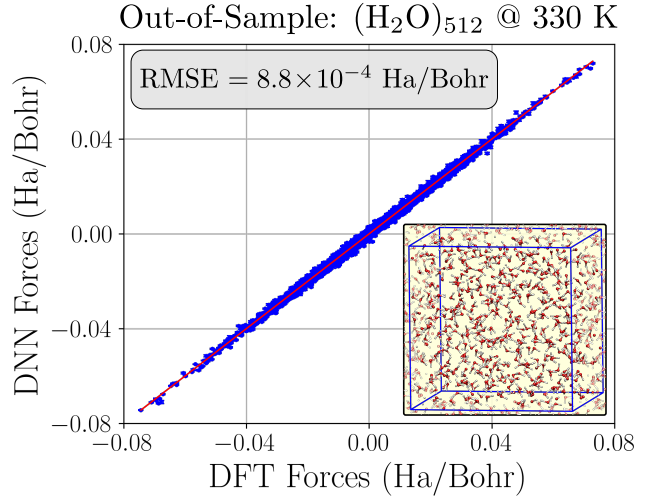


FIG. 5. Correlation plot between the ionic force components computed with the SeA-trained DNN model (trained on  $(\text{H}_2\text{O})_{64}$  at 300 K and 1 Bar at the PBE0 level) and the ground-truth PBE0 ionic force components directly computed using SeA for an out-of-sample test set containing two uncorrelated snapshots from a DPMD simulation of  $(\text{H}_2\text{O})_{512}$  at 330 K and 1 Bar. The DNN ionic force components are plotted as blue dots (with error bars based on the mean and standard deviation among the four independently trained DNN models), while the red line indicates perfect correlation with the ground-truth ionic force components.

formed in Sec. IV A at  $T = 300$  K and 1 Bar (i.e., the training/active-learning thermodynamic condition). When compared against direct ionic force calculations with SeA, we found that the ionic forces furnished by the final DNN model(s) are highly accurate with a RMSE of  $7.3 \times 10^{-4}$  Ha/Bohr. For a more stringent test, we also prepared an out-of-sample test set, which included two equispaced snapshots from an  $\approx 1$  ns DPMD simulation of  $(\text{H}_2\text{O})_{512}$  at  $T = 330$  K and 1 Bar (using the DNN potential trained on  $(\text{H}_2\text{O})_{64}$  at  $T = 300$  K and 1 Bar). Using these uncorrelated snapshots, we again found that the ionic forces provided by the DNN model(s) were able to reproduce the ground-truth ionic forces with very high fidelity (Fig. 5). As depicted in this figure, the RMSE for this test set (which is out-of-sample in both system size and  $T$ ) was  $8.8 \times 10^{-4}$  Ha/Bohr, which is only slightly larger than the RMSE ( $7.3 \times 10^{-4}$  Ha/Bohr) found above for  $(\text{H}_2\text{O})_{64}$  snapshots collected at the training/active-learning thermodynamic condition. We attribute this (rather small) RMSE increase to the additional structural disorder afforded by the extended system size ( $(\text{H}_2\text{O})_{64} \rightarrow (\text{H}_2\text{O})_{512}$ ) and elevated temperature (300 K  $\rightarrow$  330 K) in the out-of-sample test set. Here, we also note that both RMSE values are below typical force convergence thresholds ( $\sim 10^{-3}$  Ha/Bohr), which further highlights the high degree of accuracy achieved by this DNN model.

Besides validating the accuracy of our SeA-trained DNN model, the direct calculations of the ionic forces in

these two  $(\text{H}_2\text{O})_{512}$  snapshots (each containing  $> 1,500$  atoms) using SeA also highlight the capability of this approach when performing hybrid DFT calculations of large-scale condensed-phase systems. For such challenging systems (which are currently beyond the reach of PWSCF (ACE)), SeA enabled us to perform fully self-consistent calculations of the energies and ionic forces at the hybrid DFT level in  $\approx 4.5$  hours using 300 Cori-KNL nodes (with 1 MPI process and 68 OpenMP threads per node). Not only are these calculations made possible using SeA, but the overall cost of these calculations is again dominated by the cost-efficient inner-loop SCF\_Iteration steps instead of the cost-prohibitive outer-loop ACE\_Construction steps in the ACE-based SCF procedure (Algorithm 1). By harnessing three levels of computational savings, SeA has effectively removed the computational bottleneck that typically prohibits the routine use of hybrid DFT in high-throughput applications for systems like  $(\text{H}_2\text{O})_{64}$  (cf. Table I) and beyond, e.g.,  $(\text{H}_2\text{O})_{512}$ . This observation again reiterates the need for more scalable GGA-based KS-DFT algorithms (e.g., linear-scaling and/or real-space approaches) that could be used in conjunction with SeA to enable the treatment of even larger systems at the hybrid DFT level.

## V. CONCLUSIONS AND FUTURE OUTLOOK

In this work, we have developed SeA (SeA = SCDM+exx+ACE)—a robust, accurate, and computationally efficient framework for performing high-throughput hybrid DFT calculations on large-scale finite-gap systems—by combining and seamlessly integrating: (i) the selected columns of the density matrix (SCDM) approach<sup>35</sup> (a direct/non-iterative orbital localization scheme that sidesteps the need for system-dependent optimization protocols), (ii) a recently extended black-box version<sup>62</sup> of exx<sup>47,49</sup> (a linear-scaling real-space EXX algorithm that exploits the sparsity between localized orbitals when evaluating the action of the standard/full-rank EXX operator ( $\hat{V}_{\text{xx}}$ )), and (iii) adaptively compressed exchange (ACE)<sup>36</sup> (an efficient low-rank  $\hat{V}_{\text{xx}}$  approximation that eliminates unnecessary full-rank evaluations of the action during the iterative SCF procedure). By construction, SeA is able to harness three distinct levels of computational savings during hybrid DFT calculations: two from SCDM+exx (*pair selection* and *domain truncation*: as this approach only considers spatially overlapping orbital pairs and evaluates their corresponding EXX interaction on orbital-pair-specific/system-size-independent real-space domains) and one from ACE (*low-rank  $\hat{V}_{\text{xx}}$  approximation*: as this approach reduces the number of SCDM+exx calls during the SCF solution to the KS-DFT equations). To assess the accuracy and performance of SeA, we compared this approach against PWSCF (ACE) (the convolution-based ACE implementation in the PWSCF module of Quantum ESPRESSO (QE)) across a diverse test set containing 200 non-equilibrium

$(\text{H}_2\text{O})_{64}$  configurations (which include both intact and auto-ionized water molecules, and have system densities ranging from  $\approx 0.5 \text{ g/cm}^3$  to  $\approx 1.5 \text{ g/cm}^3$ ). In doing so, we found that SeA furnishes an order-of-magnitude ( $\approx 20\times$ ) speedup in the rate-determining ACE\_Construction steps in PWSCF (ACE), while reproducing the EXX energy and ionic forces with high fidelity (i.e., median (maximum) errors of  $5.2 \times 10^{-3}\%$  ( $1.1 \times 10^{-2}\%$ ) in the energy and RMSE (maximum) errors of  $1.1 \times 10^{-4} \text{ Ha/Bohr}$  ( $5.5 \times 10^{-4} \text{ Ha/Bohr}$ ) in the ionic force components). Hence, SeA effectively removes the computational bottleneck that typically prohibits the routine use of hybrid DFT in high-throughput applications involving systems with sizes similar to (and beyond)  $(\text{H}_2\text{O})_{64}$ , and enables single-point energy and ionic force evaluations for such systems with an order-of-magnitude overall speedup compared to PWSCF (ACE) and a two-order-of-magnitude overall speedup compared to the conventional (non-ACE) convolution-based EXX implementation. With ionic force errors that are lower than the typical convergence thresholds (e.g.,  $10^{-3} \text{ Ha/Bohr}$ ) used during the structural relaxation of condensed-phase systems and order-of-magnitude performance improvements, SeA paves the way towards the routine use of hybrid DFT in large-scale high-throughput applications such as materials screening and discovery, PES sampling, and quantum mechanical data generation for ML.

As a proof-of-principle high-throughput application, we used SeA to train a deep neural network (DNN) potential for ambient ( $T = 300 \text{ K}$ ,  $p = 1 \text{ Bar}$ ) liquid water at the hybrid (PBE0) DFT level, based on an actively learned data set containing  $\approx 8,000$   $(\text{H}_2\text{O})_{64}$  configurations. The convergence/precision of this SeA-trained DNN model was demonstrated by small model deviations in the ionic forces for liquid water under ambient ( $T = 300 \text{ K}$ ,  $p = 1 \text{ Bar}$ ) and non-ambient/out-of-sample ( $T \in \{270 \text{ K}, 330 \text{ K}, 360 \text{ K}\}$ ,  $p = 1 \text{ Bar}$ ) thermodynamic conditions. By comparing its ionic force predictions to the ground truth (direct hybrid DFT calculations using SeA) for a more challenging out-of-sample test set ( $(\text{H}_2\text{O})_{512}$  at  $T = 330 \text{ K}$ ,  $p = 1 \text{ Bar}$ ), we also found that the SeA-trained DNN model was highly accurate with an RMSE of  $8.8 \times 10^{-4} \text{ Ha/Bohr}$  in the ionic force components. This ground-truth comparison not only validated the accuracy of the DNN model, but also showcased the capability of SeA to perform hybrid DFT calculations for challenging condensed-phase systems containing  $> 1,500$  atoms.

While SeA in its current form already provides a robust, accurate, and computationally efficient framework for performing high-throughput condensed-phase hybrid DFT calculations on large-scale finite-gap systems, there still remains room for further improvement. In particular, we are actively working on the following research thrusts to enhance the features and capabilities of SeA: (i) support for general Monkhorst-Pack (i.e., beyond  $\Gamma$ -point) Brillouin zone sampling, (ii) an extension to range-separated hybrid (RSH) functionals,<sup>82–88</sup> and (iii)



the development of a fully real-space SeA algorithm for implementation in real-space codes. We are also actively working to further improve the overall efficiency of SeA (by enabling GPU support and reducing the prefactor in the SCDM orbital localization scheme) and finalizing a public release of SeA in the PWSCF module of QE.

Here, we would also emphasize that the applicability of SeA extends beyond high-throughput SCF calculations (i.e., single-point energy and ionic force evaluations) at the hybrid DFT level. For instance, SeA (in its current form) can be used to accelerate Born–Oppenheimer AIMD (BOMD) simulations, and has the potential to increase the length- and time-scales accessible by AIMD when used in conjunction with multiple time-stepping techniques<sup>89</sup> based on the ACE operator.<sup>45</sup> Due to the continuous time evolution of the trajectory during AIMD simulations, SeA is not restricted to the use of SCDM orbitals and could also be used in conjunction with other iterative localization schemes (e.g., MLWFs<sup>50,51</sup>) by keeping track of (and continuously refining<sup>53</sup>) the unitary operator connecting the local and canonical representations of the occupied space. Although not explicitly described in this work, the current version of SeA computes the EXX contribution to the cell forces/stress tensor (i.e.,  $\sigma_{xx}$ ) in real space via `exx`,<sup>49</sup> and can therefore be used to perform constant-pressure calculations at the hybrid DFT level (e.g., variable cell relaxations and  $NpH/NpT$  simulations) as well. Since the real-space evaluation of  $\sigma_{xx}$  is subject to small (but non-negligible) aliasing errors when performed in a planewave code, we are also working on an extension to SeA that will compute this quantity directly from  $\hat{V}_{xx}^{\text{ACE}}$  (in analogy to the evaluation of  $E_{xx}$  currently done in SeA via Eq. (19)).

## ACKNOWLEDGMENTS

All authors thank Anil Damle and Ju-an Zhang for helpful scientific discussions. This work was supported as part of the Center for Alkaline Based Energy Solutions (CABES), an Energy Frontier Research Center funded by the U.S. Department of Energy, Office of Science, Basic Energy Sciences at Cornell University under Award No. DE-SC0019445. In addition, RAD also gratefully acknowledges financial support from an Alfred P. Sloan Research Fellowship. This research used resources of the National Energy Research Scientific Computing Center, which is supported by the Office of Science of the U.S. Department of Energy under Contract No. DE-AC02-05CH11231.

## Appendix A: Computational Details (Electronic Structure Calculations)

For all hybrid DFT calculations (with SeA or PWSCF(ACE)), we used an in-house implementation built upon the PWSCF module of Quantum ESPRESSO (git ver-

sion: qe-7.0-rc1, in which the `vexx` function in PWSCF(ACE) can effectively exploit both MPI and OpenMP parallelization). We modeled the interactions between the valence electrons and ions (nuclei and their frozen-core electrons) using the Hamann–Schlüter–Chiang–Vanderbilt (HSCV) type norm-conserving pseudopotentials<sup>90,91</sup> distributed with the `Qbox` package.<sup>92</sup> Pseudo-wavefunctions for the valence electrons were represented using a planewave basis truncated at a maximum kinetic energy of 85 Ry. Unless otherwise specified, default settings (e.g., Davidson diagonalization, convergence thresholds, and density mixing parameters) were used throughout. For all PWSCF(ACE) calculations, the integrable divergence at  $\mathbf{G} = 0$  during `vexx` evaluations was treated using the Gygi–Baldereschi approach.<sup>20</sup> For all SeA calculations, we followed the previous `exx` settings<sup>47,49</sup> for the near-field PE (e.g., sixth-order discrete Laplacian operator and conjugate gradient convergence) and far-field ME (maximum angular momentum of  $l_{\text{max}} = 6$ ). The value of  $\delta$  in `exx` (i.e., the minimum  $S_{|i,j|}$  value for determining overlapping  $\langle ij \rangle$  pairs, see discussion surrounding Eq. (17)) was automatically determined using the system-independent model discussed in Ref. 62 (assuming uniform SCDM spread and a lack of long-range structural order).

## Appendix B: Computational Details (DNN Training and DPMD Simulations)

The DeepMD-kit<sup>93</sup> (git version: v1.3.3) interfaced with the TensorFlow library<sup>94</sup> (git version: v2.4.0) was used to train the DNN model for liquid water based on the total energy  $E$  and ionic forces  $\{\mathbf{F}_I\}$  from each selected configuration in a given training set. We used DeepPot-SE<sup>81</sup> to smoothly map the local chemical environment around each atom (i.e., the relative atomic coordinates within a radius of 6 Å) into input for a DNN model containing two coupled three-layer DNNs (i.e., an embedding network with (25, 50, 100) neurons and a fitting network with (60, 60, 60) neurons). During the training/active-learning process, we followed Refs. 80 and 81 and minimized the following loss function  $\mathcal{L}$ :

$$\mathcal{L}(\lambda, \eta) = \frac{\lambda}{N^2} |\Delta E|^2 + \frac{\eta}{3N} \sum_I |\Delta \mathbf{F}_I|^2, \quad (\text{B1})$$

in which  $\Delta E$  and  $\Delta \mathbf{F}_I$  are the differences between the DPMD model prediction and the training data for  $E$  and  $\mathbf{F}_I$ , respectively, and  $N$  is the number of atoms in a given configuration. The Adam stochastic gradient descent method<sup>95</sup> was performed for 0.5 M steps to train the DPMD model parameters ( $\lambda$  and  $\eta$ ) with an initial learning rate of  $5.0 \times 10^{-3}$  that exponentially decayed with respect to the number of training steps to  $1.0 \times 10^{-8}$ . As a function of the learning rate, we linearly varied  $\lambda$  (from  $10^{-2}$  to 1) and  $\eta$  (from  $10^3$  to 1) to achieve an efficient and well-balanced training procedure.

All DPMD simulations were performed using LAMMPS<sup>96</sup> (git version: stable\_29Oct2020) with Nosé–Hoover thermostat and barostat chains<sup>97</sup> (and characteristic timescales of 0.1 ps and 0.5 ps, respectively). All hydrogen atoms were replaced with deuterium to allow for a 0.5-fs integration time step. For each temperature setting, we performed a 100-ps equilibration run followed by a 1-ns production calculation



to sample the  $NpT$  ensemble using a cubic periodic cell with

64 water molecules. Snapshots were taken every 100 DPMD steps to form a discrete trajectory for analysis.

- 
- \* distasio@cornell.edu
- <sup>1</sup> S. Curtarolo, G. L. W. Hart, M. B. Nardelli, N. Mingo, S. Sanvito, and O. Levy, “The high-throughput highway to computational materials design,” *Nat. Mater.* **12**, 191–201 (2013).
  - <sup>2</sup> O. A. von Lilienfeld, “Towards the computational design of compounds from first principles,” in *Many-Electron Approaches in Physics, Chemistry and Mathematics: A Multidisciplinary View*, Mathematical Physics Studies, edited by V. Bach and L. Delle Site (Springer International Publishing, Cham, 2014) pp. 169–189.
  - <sup>3</sup> O. T. Unke, S. Chmiela, H. E. Sauceda, M. Gastegger, I. Poltavsky, K. T. Schütt, A. Tkatchenko, and K.-R. Müller, “Machine learning force fields,” *Chem. Rev.* **121**, 10142–10186 (2021).
  - <sup>4</sup> M. Meuwly, “Machine learning for chemical reactions,” *Chem. Rev.* **121**, 10218–10239 (2021).
  - <sup>5</sup> B. Huang and O. A. von Lilienfeld, “Ab initio machine learning in chemical compound space,” *Chem. Rev.* **121**, 10001–10036 (2021).
  - <sup>6</sup> P. Hohenberg and W. Kohn, “Inhomogeneous electron gas,” *Phys. Rev.* **136**, B864 (1964).
  - <sup>7</sup> W. Kohn and L. J. Sham, “Self-consistent equations including exchange and correlation effects,” *Phys. Rev.* **140**, A1133 (1965).
  - <sup>8</sup> R. G. Parr and W. Yang, *Density-Functional Theory of Atoms and Molecules* (Oxford University Press, New York, 1989).
  - <sup>9</sup> “A primer in density functional theory,” in *Lecture Notes in Physics*, Vol. 620, edited by C. Fiolhais, F. Nogueira, and M. Marques (Springer, New York, 2003).
  - <sup>10</sup> A. D. Becke, “Perspective: Fifty years of density-functional theory in chemical physics,” *J. Chem. Phys.* **140**, 18A301 (2014).
  - <sup>11</sup> N. Mardirossian and M. Head-Gordon, “Thirty years of density functional theory in computational chemistry: An overview and extensive assessment of 200 density functionals,” *Mol. Phys.* **115**, 2315–2372 (2017).
  - <sup>12</sup> M. G. Medvedev, I. S. Bushmarinov, J. Sun, J. P. Perdew, and K. A. Lyssenko, “Density functional theory is straying from the path toward the exact functional,” *Science* **355**, 49–52 (2017).
  - <sup>13</sup> K. P. Kepp, “Comment on: density functional theory is straying from the path toward the exact functional,” *Science* **356**, 496–496 (2017).
  - <sup>14</sup> S. Hammes-Schiffer, “A conundrum for density functional theory,” *Science* **355**, 28–29 (2017).
  - <sup>15</sup> M. G. Medvedev, I. S. Bushmarinov, J. Sun, J. P. Perdew, and K. A. Lyssenko, “Response to Comment on: density functional theory is straying from the path toward the exact functional,” *Science* **356**, 496–496 (2017).
  - <sup>16</sup> S. Lehtola, C. Steigemann, M. J. T. Oliveira, and M. A. L. Marques, “Recent developments in `libxc`—a comprehensive library of functionals for density functional theory,” *SoftwareX* **7**, 1–5 (2018).
  - <sup>17</sup> J. P. Perdew and A. Zunger, “Self-interaction correction to density-functional approximations for many-electron systems,” *Phys. Rev. B* **23**, 5048–5079 (1981).
  - <sup>18</sup> A. J. Cohen, P. Mori-Sánchez, and W. Yang, “Insights into current limitations of density functional theory,” *Science* **321**, 792–794 (2008).
  - <sup>19</sup> A. D. Becke, “Density-functional thermochemistry. iii. the role of exact exchange,” *J. Chem. Phys.* **98**, 5648–5652 (1993).
  - <sup>20</sup> F. Gygi and A. Baldereschi, “Self-consistent Hartree-Fock and screened-exchange calculations in solids: Application to silicon,” *Phys. Rev. B* **34**, 4405–4408 (1986).
  - <sup>21</sup> S. Chawla and G. A. Voth, “Exact exchange in ab initio molecular dynamics: An efficient plane-wave based algorithm,” *J. Chem. Phys.* **108**, 4697–4700 (1998).
  - <sup>22</sup> A. F. Izmaylov, G. E. Scuseria, and M. J. Frisch, “Efficient evaluation of short-range hartree-fock exchange in large molecules and periodic systems,” *J. Chem. Phys.* **125**, 104103 (2006).
  - <sup>23</sup> A. Sorouri, W. M. C. Foulkes, and N. D. M. Hine, “Accurate and efficient method for the treatment of exchange in a plane-wave basis,” *J. Chem. Phys.* **124**, 064105 (2006).
  - <sup>24</sup> M. Guidon, F. Schiffmann, J. Hutter, and J. VandeVondele, “Ab initio molecular dynamics using hybrid density functionals,” *J. Chem. Phys.* **128**, 214104 (2008).
  - <sup>25</sup> M. Guidon, J. Hutter, and J. VandeVondele, “Robust periodic hartree-fock exchange for large-scale simulations using gaussian basis sets,” *J. Chem. Theory Comput.* **5**, 3010–3021 (2009).
  - <sup>26</sup> X. Wu, A. Selloni, and R. Car, “Order- $n$  implementation of exact exchange in extended insulating systems,” *Phys. Rev. B* **79**, 085102 (2009).
  - <sup>27</sup> F. Gygi, “Compact representations of kohn-sham invariant subspaces,” *Phys. Rev. Lett.* **102**, 166406 (2009).
  - <sup>28</sup> M. Guidon, J. Hutter, and J. VandeVondele, “Auxiliary density matrix methods for Hartree-Fock exchange calculations,” *J. Chem. Theory Comput.* **6**, 2348–2364 (2010).
  - <sup>29</sup> I. Duchemin and F. Gygi, “A scalable and accurate algorithm for the computation of hartree-fock exchange,” *Comput. Phys. Commun.* **181**, 855–860 (2010).
  - <sup>30</sup> E. J. Bylaska, K. Tsemekhman, S. B. Baden, J. H. Weare, and H. Jonsson, “Parallel implementation of  $\gamma$ -point pseudopotential plane-wave DFT with exact exchange,” *J. Comput. Chem.* **32**, 54–69 (2011).
  - <sup>31</sup> N. Varini, D. Ceresoli, L. Martin-Samos, I. Girotto, and C. Cavazzoni, “Enhancement of DFT-calculations at petascale: Nuclear magnetic resonance, hybrid density functional theory and Car-Parrinello calculations,” *Comput. Phys. Commun.* **184**, 1827–1833 (2013).
  - <sup>32</sup> F. Gygi and I. Duchemin, “Efficient computation of hartree-fock exchange using recursive subspace bisection,” *J. Chem. Theory Comput.* **9**, 582–587 (2013).
  - <sup>33</sup> R. A. DiStasio Jr., B. Santra, Z. Li, X. Wu, and R. Car, “The individual and collective effects of exact exchange and dispersion interactions on the *ab initio* structure of liquid water,” *J. Chem. Phys.* **141**, 084502 (2014).
  - <sup>34</sup> W. Dawson and F. Gygi, “Performance and accuracy of recursive subspace bisection for hybrid DFT calculations in inhomogeneous systems,” *J. Chem. Theory Comput.* **11**,

- 4655–4663 (2015).
- <sup>35</sup> A. Damle, L. Lin, and L. Ying, “Compressed representation of kohn-sham orbitals via selected columns of the density matrix,” *J. Chem. Theory Comput.* **11**, 1463–1469 (2015).
  - <sup>36</sup> L. Lin, “Adaptively compressed exchange operator,” *J. Chem. Theory Comput.* **12**, 2242–2249 (2016).
  - <sup>37</sup> N. M. Boffi, M. Jain, and A. Natan, “Efficient computation of the Hartree-Fock exchange in real-space with projection operators,” *J. Chem. Theory Comput.* **12**, 3614–3622 (2016).
  - <sup>38</sup> T. A. Barnes, T. Kurth, P. Carrier, N. Wichmann, D. Prendergast, P. R. C. Kent, and J. Deslippe, “Improved treatment of exact exchange in Quantum ESPRESSO,” *Comput. Phys. Commun.* **214**, 52–58 (2017).
  - <sup>39</sup> W. Hu, L. Lin, and C. Yang, “Interpolative separable density fitting decomposition for accelerating hybrid density functional calculations with applications to defects in silicon,” *J. Chem. Theory Comput.* **13**, 5420–5431 (2017).
  - <sup>40</sup> W. Hu, L. Lin, and C. Yang, “Projected commutator DIIS method for accelerating hybrid functional electronic structure calculations,” *J. Chem. Theory Comput.* **13**, 5458–5467 (2017).
  - <sup>41</sup> J. Mountjoy, M. Todd, and N. J. Mosey, “Exact exchange with non-orthogonal generalized wannier functions,” *J. Chem. Phys.* **146**, 104108 (2017).
  - <sup>42</sup> K. Dong, W. Hu, and L. Lin, “Interpolative separable density fitting through centroidal voronoi tessellation with applications to hybrid functional electronic structure calculations,” *J. Chem. Theory Comput.* **14**, 1311–1320 (2018).
  - <sup>43</sup> I. Carnimeo, S. Baroni, and P. Giannozzi, “Fast hybrid density-functional computations using plane-wave basis sets,” *Electron. Struct.* **1**, 015009 (2019).
  - <sup>44</sup> S. Mandal, J. Debnath, B. Meyer, and N. N. Nair, “Enhanced sampling and free energy calculations with hybrid functionals and plane waves for chemical reactions,” *J. Chem. Phys.* **149**, 144113 (2018).
  - <sup>45</sup> S. Mandal and N. N. Nair, “Speeding-up *ab initio* molecular dynamics with hybrid functionals using adaptively compressed exchange operator based multiple timestepping,” *J. Chem. Phys.* **151**, 151102 (2019).
  - <sup>46</sup> S. Mandal and N. N. Nair, “Efficient computation of free energy surfaces of chemical reactions using *ab initio* molecular dynamics with hybrid functionals and plane waves,” *J. Comput. Chem.* **41**, 1790–1797 (2020).
  - <sup>47</sup> H.-Y. Ko, J. Jia, B. Santra, X. Wu, R. Car, and R. A. DiStasio Jr., “Enabling large-scale condensed-phase hybrid density functional theory based *ab initio* molecular dynamics. I. theory, algorithm, and performance,” *J. Chem. Theory Comput.* **16**, 3757–3785 (2020).
  - <sup>48</sup> S. Mandal, V. Thakkur, and N. N. Nair, “Achieving an order of magnitude speedup in hybrid-functional- and plane-wave-based *ab initio* molecular dynamics: Applications to proton-transfer reactions in enzymes and in solution,” *J. Chem. Theory Comput.* **17**, 2244–2255 (2021).
  - <sup>49</sup> H.-Y. Ko, B. Santra, and R. A. DiStasio, “Enabling large-scale condensed-phase hybrid density functional theory-based *ab initio* molecular dynamics II: Extensions to the isobaric–isoenthalpic and isobaric–isothermal ensembles,” *J. Chem. Theory Comput.* **17**, 7789–7813 (2021).
  - <sup>50</sup> N. Marzari and D. Vanderbilt, “Maximally localized generalized wannier functions for composite energy bands,” *Phys. Rev. B* **56**, 12847–12865 (1997).
  - <sup>51</sup> N. Marzari, A. A. Mostofi, J. R. Yates, I. Souza, and D. Vanderbilt, “Maximally localized wannier functions: Theory and applications,” *Rev. Mod. Phys.* **84**, 1419–1475 (2012).
  - <sup>52</sup> P. Giannozzi, O. Andreussi, T. Brumme, O. Bunau, M. B. Nardelli, M. Calandra, R. Car, C. Cavazzoni, D. Ceresoli, M. Cococcioni, N. Colonna, I. Carnimeo, A. D. Corso, S. de Gironcoli, P. Delugas, R. A. DiStasio Jr., A. Ferretti, A. Floris, G. Fratesi, G. Fugallo, R. Gebauer, U. Gerstmann, F. Giustino, T. Gorni, J. Jia, M. Kawamura, H.-Y. Ko, A. Kokalj, E. Küçükbenli, M. Lazzeri, M. Marsili, N. Marzari, F. Mauri, N. L. Nguyen, H.-V. Nguyen, A. Otero-de-la-Roza, L. Paulatto, S. Poncé, D. Rocca, R. Sabatini, B. Santra, M. Schlipf, A. P. Seitsonen, A. Smogunov, I. Timrov, T. Thonhauser, P. Umari, N. Vast, X. Wu, and S. Baroni, “Advanced capabilities for materials modelling with Quantum ESPRESSO,” *J. Phys.: Condens. Matter* **29**, 465901 (2017).
  - <sup>53</sup> M. Sharma, Y. Wu, and R. Car, “*Ab initio* molecular dynamics with maximally localized wannier functions,” *Int. J. Quantum Chem.* **95**, 821–829 (2003).
  - <sup>54</sup> X. Wu, E. J. Walter, A. M. Rappe, R. Car, and A. Selloni, “Hybrid density functional calculations of the band gap of  $\text{Ga}_{x}\text{In}_{1-x}\text{N}$ ,” *Phys. Rev. B* **80**, 115201 (2009).
  - <sup>55</sup> J. Chen, X. Wu, and A. Selloni, “Electronic structure and bonding properties of cobalt oxide in the spinel structure,” *Phys. Rev. B* **83**, 245204 (2011).
  - <sup>56</sup> B. Santra, R. A. DiStasio Jr., F. Martelli, and R. Car, “Local structure analysis in *ab initio* liquid water,” *Mol. Phys.* **113**, 2829–2841 (2015).
  - <sup>57</sup> A. Bankura, B. Santra, R. A. DiStasio Jr., C. W. Swartz, M. L. Klein, and X. Wu, “A systematic study of chloride ion solvation in water using van der Waals inclusive hybrid density functional theory,” *Mol. Phys.* **113**, 2842–2854 (2015).
  - <sup>58</sup> M. Chen, L. Zheng, B. Santra, H.-Y. Ko, R. A. DiStasio Jr., M. L. Klein, R. Car, and X. Wu, “Hydroxide diffuses slower than hydronium in water because its solvated structure inhibits correlated proton transfer,” *Nat. Chem.* **10**, 413–419 (2018).
  - <sup>59</sup> H.-Y. Ko, R. A. DiStasio Jr., B. Santra, and R. Car, “Thermal expansion in dispersion-bound molecular crystals,” *Phys. Rev. Materials* **2**, 055603 (2018).
  - <sup>60</sup> H.-Y. Ko, L. Zhang, B. Santra, H. Wang, W. E. R. A. DiStasio Jr., and R. Car, “Isotope effects in liquid water via deep potential molecular dynamics,” *Mol. Phys.* **117**, 3269–3281 (2019).
  - <sup>61</sup> R. Car and M. Parrinello, “Unified approach for molecular dynamics and density-functional theory,” *Phys. Rev. Lett.* **55**, 2471–2474 (1985).
  - <sup>62</sup> Z. M. Sparrow, H.-Y. Ko, and R. A. DiStasio Jr., “Enabling linear scaling exact exchange for heterogeneous systems,” (in prep).
  - <sup>63</sup> J. P. Perdew, M. Ernzerhof, and K. Burke, “Rationale for mixing exact exchange with density functional approximations,” *J. Chem. Phys.* **105**, 9982–9985 (1996).
  - <sup>64</sup> C. Adamo and V. Barone, “Toward reliable density functional methods without adjustable parameters: The PBE0 model,” *J. Chem. Phys.* **110**, 6158–6170 (1999).
  - <sup>65</sup> A. Damle, L. Lin, and L. Ying, “Scdm-*k*: Localized orbitals for solids via selected columns of the density matrix,” *J. Comput. Phys.* **334**, 1–15 (2017).
  - <sup>66</sup> W. Kohn, “Density functional and density matrix method scaling linearly with the number of atoms,” *Phys. Rev. Lett.* **76**, 3168–3171 (1996).

- <sup>67</sup> E. Prodan and W. Kohn, “Nearsightedness of electronic matter,” *Proc. Natl. Acad. Sci. U.S.A.* **102**, 11635–11638 (2005).
- <sup>68</sup> L. Kronik, A. Makmal, M. L. Tiago, M. M. G. Alemany, M. Jain, X. Huang, Y. Saad, and J. R. Chelikowsky, “PAR-SEC – the pseudopotential algorithm for real-space electronic structure calculations: recent advances and novel applications to nano-structures,” *Phys. Status Solidi B* **243**, 1063 (2006).
- <sup>69</sup> L. Zhang, D.-Y. Lin, H. Wang, R. Car, and W. E, “Active learning of uniformly accurate interatomic potentials for materials simulation,” *Phys. Rev. Materials* **3**, 023804 (2019).
- <sup>70</sup> Y. Zhang, H. Wang, W. Chen, J. Zeng, L. Zhang, H. Wang, and W. E, “DP-GEN: A concurrent learning platform for the generation of reliable deep learning based potential energy models,” *Comput. Phys. Commun.* **253**, 107206 (2020).
- <sup>71</sup> J. Sun, A. Ruzsinszky, and J. P. Perdew, “Strongly constrained and appropriately normed semilocal density functional,” *Phys. Rev. Lett.* **115**, 036402 (2015).
- <sup>72</sup> J. Sun, R. C. Remsing, Y. Zhang, Z. Sun, A. Ruzsinszky, H. Peng, Z. Yang, A. Paul, U. Waghmare, X. Wu, M. L. Klein, and J. P. Perdew, “Accurate first-principles structures and energies of diversely bonded systems from an efficient density functional,” *Nat Chem* **8**, 831–836 (2016).
- <sup>73</sup> M. Chen, H.-Y. Ko, R. C. Remsing, M. F. C. Andrade, B. Santra, Z. Sun, A. Selloni, R. Car, M. L. Klein, J. P. Perdew, and X. Wu, “Ab initio theory and modeling of water,” *Proc. Natl. Acad. Sci. U.S.A.* **114**, 10846–10851 (2017).
- <sup>74</sup> L. Zheng, M. Chen, Z. Sun, H.-Y. Ko, B. Santra, P. Dhuvad, and X. Wu, “Structural, electronic, and dynamical properties of liquid water by ab initio molecular dynamics based on SCAN functional within the canonical ensemble,” *J. Chem. Phys.* **148**, 164505 (2018).
- <sup>75</sup> C. Andreani, G. Romanelli, A. Parmentier, R. Senesi, A. I. Kolesnikov, H.-Y. Ko, M. F. Calegari Andrade, and R. Car, “Hydrogen dynamics in supercritical water Probed by neutron scattering and computer simulations,” *J. Phys. Chem. Lett.* **11**, 9461–9467 (2020).
- <sup>76</sup> M. F. Calegari Andrade, H.-Y. Ko, R. Car, and A. Selloni, “Structure, polarization, and sum frequency generation spectrum of interfacial water on anatase TiO<sub>2</sub>,” *J. Phys. Chem. Lett.* **9**, 6716–6721 (2018).
- <sup>77</sup> M. F. Calegari Andrade, H.-Y. Ko, L. Zhang, R. Car, and A. Selloni, “Free energy of proton transfer at the water–tio<sub>2</sub> interface from ab initio deep potential molecular dynamics,” *Chem. Sci.* **11**, 2335–2341 (2020).
- <sup>78</sup> L. Zhang, H. Wang, R. Car, and W. E, “Phase diagram of a deep potential water model,” *Phys. Rev. Lett.* **126**, 236001 (2021).
- <sup>79</sup> J. P. Perdew, K. Burke, and M. Ernzerhof, “Generalized gradient approximation made simple,” *Phys. Rev. Lett.* **77**, 3865–3868 (1996).
- <sup>80</sup> L. Zhang, J. Han, H. Wang, R. Car, and W. E, “Deep potential molecular dynamics: A scalable model with the accuracy of quantum mechanics,” *Phys. Rev. Lett.* **120**, 143001 (2018).
- <sup>81</sup> L. Zhang, J. Han, H. Wang, W. Saidi, R. Car, and W. E, “End-to-end symmetry preserving inter-atomic potential energy model for finite and extended systems,” in *Advances in Neural Information Processing Systems 31*, edited by S. Bengio, H. Wallach, H. Larochelle, K. Grauman, N. Cesa-Bianchi, and R. Garnett (Curran Associates, Red Hook, 2018) pp. 4436–4446.
- <sup>82</sup> J. Heyd, G. E. Scuseria, and M. Ernzerhof, “Hybrid functionals based on a screened coulomb potential,” *J. Chem. Phys.* **118**, 8207–8215 (2003).
- <sup>83</sup> I. C. Gerber and J. G. Ángyán, “Hybrid functional with separated range,” *Chem. Phys. Lett.* **415**, 100–105 (2005).
- <sup>84</sup> O. A. Vydrov and G. E. Scuseria, “Assessment of a long-range corrected hybrid functional,” *J. Chem. Phys.* **125**, 234109 (2006).
- <sup>85</sup> B. G. Janesko, T. M. Henderson, and G. E. Scuseria, “Screened hybrid density functionals for solid-state chemistry and physics,” *Phys. Chem. Chem. Phys.* **11**, 443–454 (2009).
- <sup>86</sup> R. Baer, E. Livshits, and U. Salzner, “Tuned range-separated hybrids in density functional theory,” *Annu. Rev. Phys. Chem.* **61**, 85–109 (2010).
- <sup>87</sup> L. Kronik, T. Stein, S. Refaely-Abramson, and R. Baer, “Excitation gaps of finite-sized systems from optimally tuned range-separated hybrid functionals,” *J. Chem. Theory Comput.* **8**, 1515–1531 (2012).
- <sup>88</sup> A. Karolewski, L. Kronik, and S. Kümmel, “Using optimally tuned range separated hybrid functionals in ground-state calculations: Consequences and caveats,” *J. Chem. Phys.* **138**, 204115 (2013).
- <sup>89</sup> M. Tuckerman, B. J. Berne, and G. J. Martyna, “Reversible multiple time scale molecular dynamics,” *J. Chem. Phys.* **97**, 1990–2001 (1992).
- <sup>90</sup> D. R. Hamann, M. Schlüter, and C. Chiang, “Norm-conserving pseudopotentials,” *Phys. Rev. Lett.* **43**, 1494–1497 (1979).
- <sup>91</sup> D. Vanderbilt, “Optimally smooth norm-conserving pseudopotentials,” *Phys. Rev. B* **32**, 8412–8415 (1985).
- <sup>92</sup> F. Gygi, “Architecture of Qbox: A scalable first-principles molecular dynamics code,” *IBM J. Res. Dev.* **52**, 137–144 (2008).
- <sup>93</sup> H. Wang, L. Zhang, J. Han, and W. E, “DeePMD-kit: A deep learning package for many-body potential energy representation and molecular dynamics,” *Comput. Phys. Commun.* **228**, 178–184 (2018).
- <sup>94</sup> M. Abadi, P. Barham, J. Chen, Z. Chen, A. Davis, J. Dean, M. Devin, S. Ghemawat, G. Irving, M. Isard, M. Kudlur, J. Levenberg, R. Monga, S. Moore, D. G. Murray, B. Steiner, P. Tucker, V. Vasudevan, P. Warden, M. Wicke, Y. Yu, and X. Zheng, “Tensorflow: A system for large-scale machine learning,” in *12th USENIX Symposium on Operating Systems Design and Implementation (OSDI 16)* (2016) pp. 265–283.
- <sup>95</sup> D. Kingma and J. Ba, “Adam: a method for stochastic optimization,” in *Proceedings of the International Conference on Learning Representations (ICLR)* (2015).
- <sup>96</sup> S. Plimpton, “Fast parallel algorithms for short-range molecular dynamics,” *J. Comput. Phys.* **117**, 1–19 (1995).
- <sup>97</sup> M. E. Tuckerman, J. Alejandre, R. López-Rendón, A. L. Jochim, and G. J. Martyna, “A liouville-operator derived measure-preserving integrator for molecular dynamics simulations in the isothermal–isobaric ensemble,” *J. Phys. A: Math. Gen.* **39**, 5629–5651 (2006).